THESIS

SINGLE-SHOT FLASH IMAGING USING A COMPACT SOFT X-RAY MICROSCOPE

Submitted by

Sergio Carbajo

Department of Electrical and Computer Engineering

In partial fulfillment of the requirements

For the Degree of Master of Science

Colorado State University

Fort Collins, Colorado

Spring 2012

Master's Committee:

Advisor: Carmen S. Menoni

Jorge J. Rocca
Mario C. Marconi
Diego Krapf
Alan K. Van Orden

ABSTRACT

SINGLE-SHOT FLASH IMAGING USING
A COMPACT SOFT X-RAY MICROSCOPE

Microscopes extend the ability of our eyes to see objects at micro- and nanoscales. There are applications, however, for which a static image is not sufficient, and thus require information on the dynamics before a process can be understood and controlled. Therefore, the visualization of nanoscale dynamics in real-space can significantly contribute to the understanding of nanoscale processes and to accelerate the development of new nanodevices. Today, there is a need for practical microscopes capable of delivering nanometer spatial resolution and ultrafast temporal resolution in order to readily visualize any arbitrary nanoscale phenomenon. Conventional visible light microscopes can visualize ultrafast dynamics but are inherently limited in spatial resolution to about 200 nm. Alternatively, transmission electron microscopes can routinely provide atomic spatial resolutions of static samples. Probing dynamics is possible using stroboscopic schemes with nanosecond temporal resolution or scanning methods which can obtain femtosecond temporal resolution at the expense of hours-long image acquisition times.

Soft x-rays (SXR) microscopes provide the ability to resolve at the nanoscale and at the same time image dynamics with nanosecond to picosecond time resolution. Pioneering work has been carried out using synchrotron illumination that has allowed to study repetitive phenomena in magnetic materials. There are however processes that are statistically reproducible but individually non-recurring that require SXR flash illumination to capture their dynamics.

SXR flash imaging requires a large number of photons per pulse to illuminate the sample (about 10E12 photons per pulse). There are two types of SXR sources presently available which offer such high peak brightness: free electron lasers

(FEL) and table-top SXR lasers. FELs have been used to probe dynamics using holographic and diffractive imaging configurations. This thesis describes the first demonstration of real-space flash imaging using a compact SXR laser operating at a wavelength of 46.9 nm. A sequence of flash images obtained with the full-field SXR microscope with a spatial resolution of 50 nm and temporal resolution of 1.5 ns captured the interaction dynamics of a rapidly oscillating magnetic tip in close proximity to a magnetized surface. The interaction of the tip and the stray magnetic fields led to changes in the amplitude of the tip oscillation as small as 30 nm. Modeling of the interaction assuming an undamped perturbed harmonic oscillator corroborate the experimental results. The use of compact plasma-based SXR lasers operating at wavelengths down to 10.9 nm will allow to capture flash images and render animations of picosecond phenomena with a few nanometers accuracy on a table-top.

ACKNOWLEDGEMENTS

I extend my deepest gratitude to my advisor Professor Carmen S. Menoni, to whom I entirely owe my debut in research as a way of living. She has unconditionally supported me and my work personally, professionally, and financially. For that I will always be grateful. I also enjoy chatting with her and unwinding over Spanish monarchy tabloids.

I would also like to express my gratitude to my committee members for their input and insightful comments. To Professor Jorge J. Rocca, for his incessant encouragement to pursue the impossible. He has definitely pulled the imaging wagon in our lowest times. To Professor Mario C. Marconi, for his friendly but yet extraordinarily enlightening attitude towards our research. To Professor Diego Krapf, whom I have had the pleasure to be guided by, specially during my very early beginnings at Colorado State University.

Thanks to Professor Kristen S. Buchanan, for strongly adding comprehensively to the conception of the experimental demonstration of this thesis and helping me understand the underlying physics.

Cross-path past and present members and friends of the imaging team, a list that does not really extend too long. Fernando Brizuela greatly contributed to the initial development of the experiment. I can very securely assure that he might be the friendliest mentor I will encounter in my life. To him I owe the daily morning NPR podcasting habit. Isela Howlett and I took an infinite amount of data hand in hand. She also had to cope with my moods and rotting coffee spills. My depleting nourishment was and continues to be mitigated by her extraordinary baking aptitudes. Thanks guys.

My experience at the ERC and Colorado has been enriched by exceptional people and my mind is overfilled with great memories. Fortunately, you are too

many to thank, so if I have ever bought you a beer or offered to do so, consider yourself part of my family.

About that, it is your unconditional pride and love what drives any achievements I make in life. But it is only in your unconditional support through my failures where I find relief. I love you.

Aita ta amari,

TABLE OF CONTENTS

Chapter 1

Imaging at the micro- and nano-scales

Microscopy has evolved to become today an extensive field of research. Microscopy carries a long history and its universality may arguably proclaim the microscope to be the most utilized tool in science, as a unique breed with the capability to bring answers to multiple applications across many different fields.

Lenses were well known long before any telescopic or microscopic effect was discovered. By the end of the thirteenth century, glass-makers had already developed glass-grinding and -polishing techniques finely enough to produce commonly used cumbersome magnifying lenses for reading. Nevertheless, it was not until the very beginning of the seventeenth century that two Dutch spectacle-makers came across the realization that an object appeared greatly magnified when experimenting with several lenses in a tube. Only a year after and inspired by these experiments, Galileo Galilei drafts the principles of lenses and builds a better instrument with a focusing device. The first publication on microscopy, *Micrographia* [1], comes out a few decades later in the hands of Robert Hooke, irrevocable pioneer and often credited with inventing the first compound microscope. Motivated by his work, Anton van Leeuwenhoek, self-taught lens maker, revolutionizes biological studies by imaging for the first time cells and bacteria. With the microscope brought to

the attention of the scientific community, four centuries of extraordinary technical innovations and achievements followed.

In 1878 Erns Abbe establishes the theoretical foundations of light microscopy and eight years later, together with Carl Zeiss, demonstrates the first diffraction-limited microscope [2, 3]. On account of the understanding of the recently formulated theory, microscopy rapidly branches out, bringing to light Nobel Prize awarded discoveries, such as the ultramicroscope for the study of colloids [4], and the phase-contrast microscope for colorless samples [5, 6].

Beyond the optical range, the desire to observe features smaller than those visible-light microscopy can resolve motivated scientist to investigate the use a particle beam of electrons as illumination, leading to the invention of the greatest resolving power microscope, the electron microscope [7].

Microscopy has evolved in complexity, attained outstanding results and reached unimaginable extents. This chapter discusses where this field stands now and reviews the leading technologies and imaging modalities.

In microscopy, it is all about the ability to distinguish the smallest possible physical details on a sample. The characteristics of the optical system in a full-field microscope determine the spatial resolution. The optical response of the sample at the illumination wavelength determines the contrast. Both resolution and contrast are essential in microscopy. Conventionally, the best achievable lateral resolution for a visible-light bright-field microscope using immersion optics is about 0.44 λ, where λ is the wavelength of illumination, which typically leads to a theoretical limit of 200 nm [8], although sub-100 nm spatial resolution has recently been demonstrated for the first time with visible light by Mosk et al. in the Netherlands [9]. With the invention of the confocal microscope [10], the depth resolution can be achieved to enable optical sectioning and 3D-reconstruction of thick specimens. One of the main disadvantages of visible-light microscopy is the

lack of natural absorption contrast. For instance, most biological specimens lack sufficient absorption contrast in the visible range and cannot be studied without the use stains. There are two main ways to overcome this limitation: (1) increase the absorption by changing the specimen properties, as in fluorescence microscopy; and (2) exploit the phase as it is the case in phase-contrast imaging [5, 6], and differential interference contrast imaging [11].

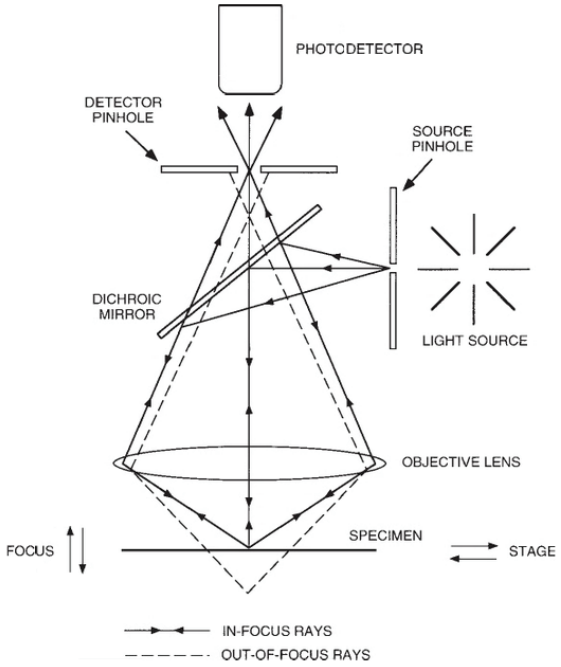

Figure 1.1: Light path in a stage **confocal microscope** [12].

Efforts to improve the spatial resolution of microscopes from micrometers to nanometers led to the invention of the electron microscope (EM) in 1931 by by Knoll and Ruska [7]. An electron microscope uses high-energy electrons with a de Broglie wavelength much shorter than the wavelength of visible light. A transmission electron microscope can in principle achieve atomic spatial resolution. EMs need to be operated in vacuum because the mean free path of electrons in air is short, of the order of a few centimeters at the most. In the case of transmission electron microscopy (TEM), the samples require additional thinning to a few tens of nanometers [13]. EM is not exempt from staining either. TEMs

commonly utilize high atomic number stains to enhance contrast, while scanning electron microscopes (SEM) require specimens to be electrically conductive at the surface in order to prevent charging, increase signal, and enhance surface resolution [14]. Any conventional sample processing technique, such as staining, drying, sectioning, or freezing often introduce artefacts that obscure the interpretation of the obtained micrographs. EM of specimens in their native state is slowly becoming more accessible through the use of specialized chambers. In a liquid cell system, usually made of thin silicon nitride membranes, the hydrated sample is maintained in a steady liquid compartment or even with a flow channel. A few experiments have demonstrated this approach that envisions a method for *in situ* studies of nanoscale structures in varying chemical environments [15, 16]. As of today, the TEM is the most powerful instrument in terms of spatial resolution with demonstrated sub-50 pm spatial resolution [17].

It is possible to achieve nanometer spatial resolution with microscopes that use as illumination radiation of much shorter wavelength, i.e. in the X-ray region. The announcement of a range of the electromagnetic spectrum with a wavelength much shorter than the visible light came in 1895 from Wilhelm Conrad Röntgen [18]. This radiation exhibited new properties in that it would penetrate most matter and thereby make internal structures visible. Since then, X-ray microscopy has established a benchmark as a solution to high resolution imaging technique. The major difference between X-ray microscopy and other techniques discussed previously is that contrast at X-ray wavelegths results from the interaction of the radiation with inner-shell electrons. Moreover, unlike EM, X-rays can provide direct chemical specificity and polarization sensitivity. Therefore, X-ray imaging combines some of the desirable capabilities from visible light microscopy while simultaneously offering an order of magnitude greater resolution, simply because the spatial resolution is proportional to the wavelength of illumination.

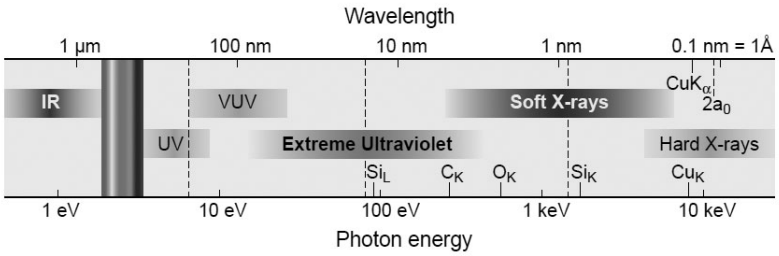

Figure 1.2: The short wavelength region of the electromagnetic spectrum: X-ray region [20].

In X-ray microscopy absorption and phase contrast arise from the interaction of the high energy photons with inner-shell electrons. These contrast mechanisms are crucial. The presence of many elemental absorption edges in the SXR region has incentivated the development of SXR full-field microscopes that can image structures with nanoscale spatial resolution [19].

The X-ray region is commonly divided into three different sub-regions: hard X-rays, with wavelengths from 0.1 Å to 3 Å (125 keV - 4 keV); soft X-rays (SXR), with wavelengths between 3 Å and 5 nm (4 keV - 250 eV); and extreme ultraviolet (EUV), ranging from 5 to 50 nm (250 eV - 25 eV). Several imaging geometries have been demonstrated to exploit the short wavelength of X-rays and achieve nanoscale resolution. The following section describes themost established X-ray imaging methods.

1.1 X-ray Imaging

1.1.1 X-ray Projection

X-ray projection is a method by which an image is created when illuminating a sample and recording the transmitted radiation, some of which is absorbed through the sample, and then recorded on an X-ray sensitive detector. This technique is the most common of all X-ray imaging techniques, including the widely known projection radiography [21]. The magnification of the object in the detec-

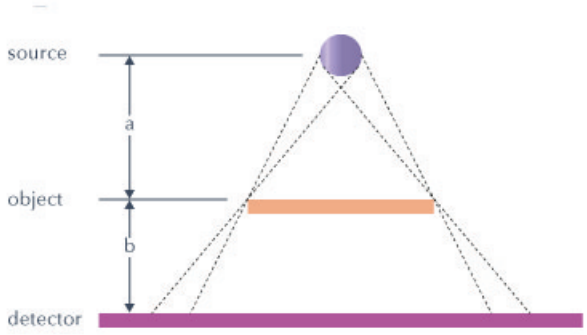

Figure 1.3: Schematic of X-ray projection imaging. The effect of edge unsharpening due to a finite size X-ray source is represented [22].

tor is achieved by positioning the sample close to a point-source of X-rays. That magnification is equal to the ratio of the source-detector and source-object distances. Because there is no imaging lens involved in the process, the resolution of the image is dependent on the magnification and the detector sensitivity; and ultimately limited by the size of the X-ray source and the resolution of the X-ray detector system, which leads to typical resolution no better than a few millimeters.

The reconstruction of 3D structures is possible through tomographic reconstruction algorithms [23], that is, by processing subsequently acquired projection images at different angles. Phase contrast can also be attained in projection imaging [24]. A theoretical formulation of X-ray phase imaging with a monochromatic point source and a phase retrieval method was first presented by Gureyev and Wilkins [25]. The combination of both, tomographic phase-contrast X-ray imaging, has also been succesfully implemented using different approaches [26, 27].

1.1.2 Scanning X-ray Microscopy

In a scanning mode, a focusing lens is used to focus an X-ray beam to a spot, often called probe, through which the specimen is raster-scanned. At each probe position, there are multiple signals that can be detected in order to map the

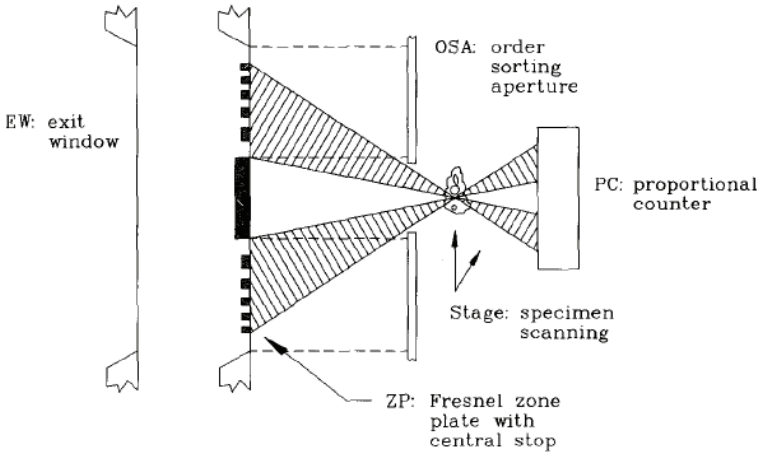

Figure 1.4: The scanning transmission X-ray microscope [30]. Schematic of the microscope showing the exit window (EW) through which beam emerges from the beamline vacuum system, the zone plate (ZP) with 0 and + 1 focal orders indicated, the order selecting aperture (OSA), the specimen mounted on a scanning stage (Stage), and the proportional counter X-ray detector (PC).

chemical, elemental or crystallographic properties of the specimen. These signals are usually the transmitted X-ray beam, fluorescent photons, photoelectrons and diffracted X-rays. Since this technique requires the employment of high intensity and collimated X-ray beams, the use of scanning X-ray microscopes has typically been limited to synchrotrons [28, 29].

This technique relies on measuring the transmitted intensity at each raster point. Therefore, it provides a map of the specimen's response to the X-ray illumination and the resolution is limited by the spot size on the specimen. Increase in resolution thus largely depends on improving focusing optics, and it is no better than several tens of nanometers [31].

1.1.3 Lens-based Full-field X-ray Microscopy

The principle of operation of a lens-based full-field X-ray microscope is analogous to that of conventional microscopes. Therefore, these microscopes capture directly a real-space image of the illuminated specimen within the field-of-view. The field-

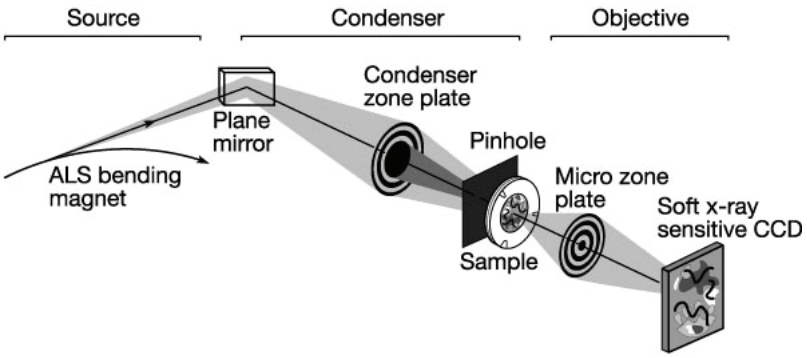

Figure 1.5: Conventional transmission zone-plate based full-field X-ray microscopy using wiggler as the illumination source [20].

of-view will decrease proportional to the quadrature of the magnification of the microscope.

The incoming X-rays from the source are tightly focused onto the sample using a condenser lens. The transmitted, scattered or reflected beam is collected by an objective lens, which forms an image onto an area detector. In this geometry, the spatial resolution is dependent on the wavelength of illumination, the numerical aperture (NA) of the objective lens and other illuminating conditions. Multiple lens-based schemes have been demonstrated employing diffractive optics [32, 33], reflective optics [34, 35], and a combination of both [36]. To date, Chao et al. have extended the spatial resolution of lens-based microscopes through a novel nanofabrication process and achieved spatial resolutions equal to the outer zone width (10 nm) of the employed zone plates [37].

1.1.4 Lensless X-ray Imaging

The difficulties in accessing optics has motivated the implementation of lensless imaging schemes such as holography and coherent diffractive imaging. This group of imaging methods has demonstrated sub-100 nm spatial resolutions in various schemes [38, 39, 40].

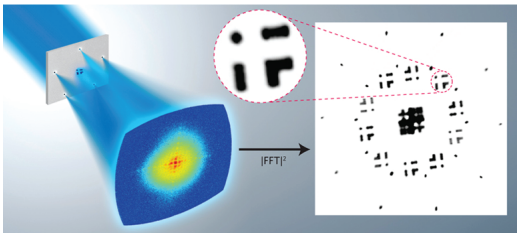

Figure 1.6: Schematic of multiple aperture Fourier transform X-ray holography [41].

Holography was invented over 65 years ago by the physicist Dennis Gabor [42]. In X-ray holography, an X-ray beam illuminates an object, which scatters the light onto a detector such as a photographic plate, while an identical copy of the initial beam, called reference beam, shines directly on the detector. The scattered light from the object form interference patterns with the non-scattered light waves from the reference beam, which serves to reconstruct an image of the object. There is a wide variety of holographic methods demonstrated to date using X-rays featuring exceptional temporal and spatial resolutions [43, 44].

X-ray coherent diffractive imaging (CDI) is another imaging method that does not require the use of lenses. In CDI, a highly coherent beam of X-rays is scattered by the sample object and produces a diffraction pattern collected by a detector [45, 38, 46]. As the detector only records the intensity of the scattered light in the far-field, the phase is retrieved through an iterative feedback algorithm. A real-space image is recovered from the diffraction pattern in the reciprocal-space with extensive post-processing. For X-ray imaging, this technique overcomes the limitations of nanofabrication processes for optics, although it requires extensive digital post-processing. X-ray CDI has in the last few years received significant attention.

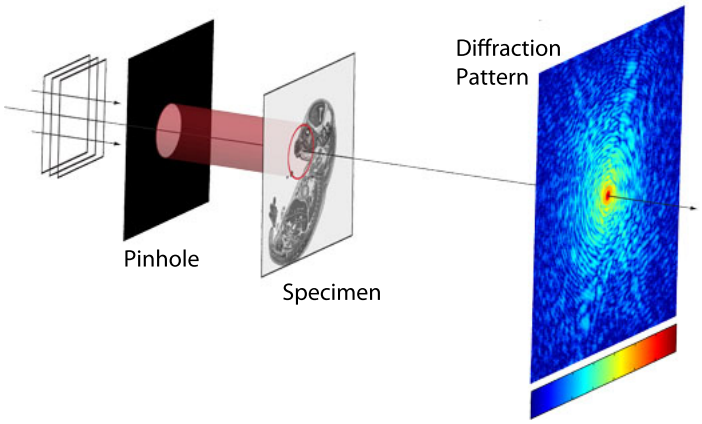

Figure 1.7: Coherent diffractive (lensless) imaging [47]. A coherent monochromatic plane-wave, limited by an aperture, is incident on a specimen. The field transmitted by the object propagates in free space and is measured by a detector array.

1.2 Temporal and Spatially Resolved Microscopy

Different fields, such as magnetic vortex dynamics [48] and the development of nano-electro-mechanical-systems (NEMS) [49], have also required the ability to capture dynamic processes. Monitoring dynamics at the nanoscale is possible with X-ray microscopy. Much of the early work in time-resolved X-ray imaging was carried out using synchrotron illumination in stroboscopic pump and probe set-ups [50, 51, 52]. As an example, by Kasai et al. [53] used this method to demonstrate current induced resonant vortex core motion in a circular Permalloy disk and to determine to polarization of the currents. These experiments have contributed to a thorough understanding of the spin torque effects (schematic shown in figure 1.2). Due to the low intensity of the X-ray pulses, these stroboscopic images were acquired over millions to billions of X-ray pulses. These stroboscopic images are bound to deterministic processes with perfect repeatability [54]. To probe dynamic processes that are statistically reproducible but individually non-recurring, pump and probe methods to to be able to capture an image using a single X-ray probe pulse.

Single ultrafast X-ray pulse acquisitions using Synchrotron sources have been demonstrated [55]. In these experiments the spatial resolution was downgraded to the micrometer range. To date, X-ray sources capable of producing short pulses with photon fluxes that enable the acquisition of nanoscale resolution images are limited to free electron lasers (FEL) and a handful of compact X-ray lasers. Only a few static images have been demonstrated thus far using single-shot X-ray pulses from any of these sources employing lens-based, holographic and diffractive schemes [36, 56, 57, 58, 59]. Moreover, stroboscopic ultrafast single-shot X-ray imaging of any dynamics has only been realized using bright flashes from a FEL [39].

Electron microscopes can also be used to observe fast dynamics. The first approach to dynamic imaging with TEM was realized in the mid 70s, by Bostanjoglo and Rosin [60], which produced stroboscopic images in TEM using beam blanking. Zewail took this idea to demonstrate a scanning imaging that uses an average of one electron per pulse with femtosecond duration created by photoexcitation of the photocathode by high-repetition femtosecond optical pulse duration laser excitation [61, 62]. The fact that there is only one electron per pulse eliminates the space-charge effects, enabling imaging spatial and temporal resolutions in the picometer and femtosecond range. Of course, this technique requires to build up the image over millions of single-electron pulses, which limits the process under study to be repeatable. The other approach to dynamic imaging is to generate pulses containing enough electrons (10^7 e^-/pulse) to construct an image from a single pulse [63]. A large number of electrons in over nanosecond pulse duration results in a very large peak current ($\gg mA$) compared to the nA in traditional TEM. Therefore, single-shot TEM suffers from limited resolution, tens of nanometers spatially and tens of nanoseconds temporally, as Coulomb interactions and repulsions lead to degradation of resolution due to stochastic blurring and global space-charge [64].

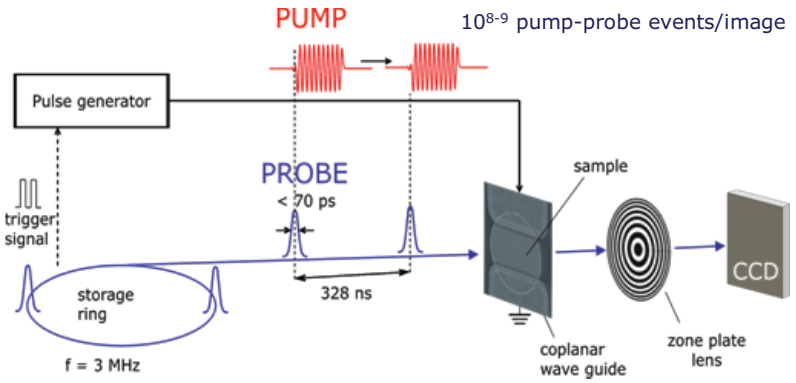

Figure 1.8: X-ray imaging schematic employed to probe spin polarization of current by current-induced magnetic vortex dynamics [53]. An average of 10^{8-9} soft X-ray pulses were required to build up an image.

1.3 Thesis Overview

The most fundamental motivation for microscopy is the ability to resolve structures that one would not be able to see with the naked eye. Microscopy is a research field by itself that brings answers to other research fields, and therefore, its advances majorly impact most areas of science and technology. Advances in this field have allowed humankind to see structures down to atomic scales [17, 65, 66]. However, recovering information on structures does not always provide all what is required to thoroughly understand a process, and it is often essential to have full information on the structural dynamics before that process can be controlled.

As illustrated in figure 1.3, there is a vast range of processes that occur in the sub-micron spatial and sub-microsecond temporal scales where there is little or no knowledge of the relevant structural dynamics. One such example is the development of complex carbon-nanotube based NEMS for which the transient behaviour in controlled processes is yet to be fully understood [49]. As another example, there is a great deal of interest in the large scale structural change of large biomolecules, such as protein folding, which occurs on the microsecond to picosencond timescales [67].

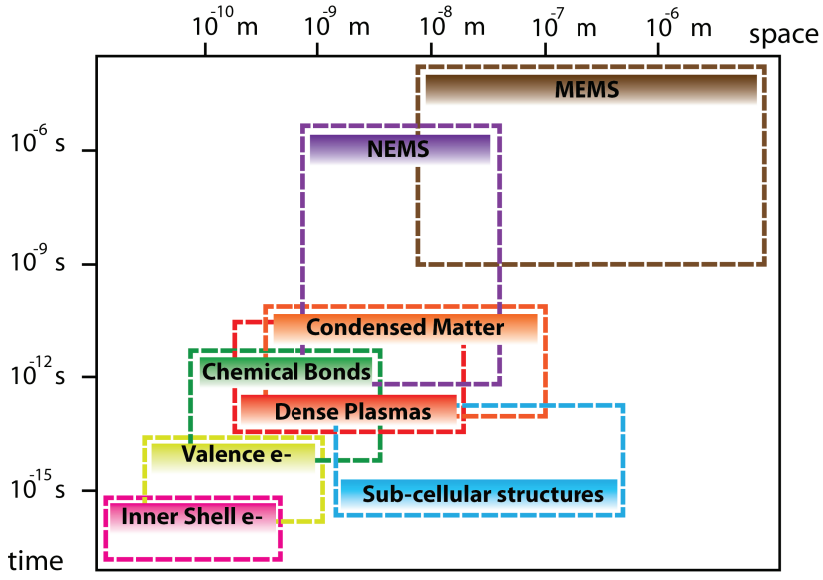

Figure 1.9: Relevant time- and spatial-scales in research areas with unknown or partially known structural dynamics.

The study of structural dynamics demands structural information at the nanoscale at the requisite temporal resolution. This calls for image acquisition in pump and probe schemes where the probe suffices the brightness required to obtain single-shot images. Of all the potential candidate probes that have access to nanoscale spatial and ultrafast temporal resolutions the only with sufficient maturity to demonstrate this capability are SXRs.

Early work in SXR imaging was carried out at Stanford by Kirkpatrick, Baez and Patee [68]. However, high spatial resolution SXR imaging was dramatically boosted only a few decades ago by the availability of bright, tunable, monochromatic soft X-ray beams from electron storage rings with demonstrations of SXR zone plate and scanning microscopy [69, 70, 71, 72, 73, 74]. Today, the available sources that provide the flux necessary to put in practice the great potential of nanoscale SXR imaging have been extended to newer generations of storage rings, linear accelerators, and compact sources, through zone plate imaging [37, 75], tomography [76, 77], holography [78, 79] and diffractive imaging [80, 81, 82, 83]. In addition to the static nanostructures, one can understand the functionality of these

nanostructures through their dynamics. The complementary effort of these techniques to coextend spatial and temporal resolutions of SXR microscopes by single flash probes will make it possible to freeze any arbitrary ultrafast phenomenon and visualize the nanoscale.

Compact SXR imaging systems offer now a unique opportunity to deliver this technology in a practical manner. This thesis describes the first demonstration of single-shot flash imaging using a compact soft X-ray microscope. In chapter 2, the theoretical foundations of SXR microscopy are described, including sources, optics, and system performance characterization methodologies. Chapter 3 is dedicated to the imaging system utilized for single-shot flash imaging demonstration. Chapter 4 briefs the details of the experiment. Finally, chapter 5 concludes with the achievements and future progress.

Chapter 2

Soft X-Ray Microscopy

As reviewed in the previous chapter, SXRs range from a few to several nanometers in wavelength and attract, therefore, much attention because of their potential for imaging with nanoscale lateral spatial resolution. This region embraces most of primary atomic resonances and absorption edges for low and intermediate z elements, from tens of eV to a few keV (tens of nanometers to a few angstroms), enabling elemental and chemical identification through natural contrast mechanisms [20, 84]. This range also exhibits magnetization sensitivity by means of spin-absorption employing circularly polarized light [85, 86]. There are several aspects that have preserved microscopy in this region of the electromagnetic spectrum relatively unexplored, specially because of the lack of practical sources and suitable optics until very recently, and in a lower degree, the late development of sensitive detectors and unfavorable vacuum demands.

In microscopy, the best achievable resolution or alternatively, minimum resolvable distance in an imaging system is described by

$$\frac{k\lambda}{NA}, \tag{2.1}$$

where λ is the wavelength of illumination NA the numerical aperture and k is a

proportionality parameter that considers various properties of the optical system. Presently, the best resolution achieved with diffractive optics is of 12 nm [37]. Soft X-ray microscopy is motivated by the potential for high resolution imaging of relatively thick samples. In biology, for instance, SXRs exploit the natural contrast mechanism of hydrated specimens without the need of stains or labels.

X-rays interact with matter in three ways: elastic scattering, inelastic scattering, and absorption. Elastic scattering is a process whereby re-emission of radiation occurs at the same frequency as the incident radiation. Elastic scattering from bound-free electrons is called Thomson scattering, while elastic scattering from bound electrons is called Rayleigh scattering. Inelastic scattering occurs when the scattering causes an electron to be ejected from the atom, thereby transferring a small fraction of the incident X-ray energy to the electron. In the soft X-ray regime, inelastic scattering is negligible and the elastic scattering cross-section is less than 1% of the absorption cross-section. Thus, the dominating process is photoelectric absorption, although inelastic scattering is important in phase-contrast imaging.

In terms of absorption, the Beer-Lambert law describes the attenuation that X-rays undergo when travelling through a material of thickness t. The intensity across t would decrease from the initial intensity I_0 according to

$$I(t) = I_0 e^{-\mu t}, \tag{2.2}$$

where μ is the linear absorption coefficient , which depends on the material's imaginary component of the refractive index (β) and the wavelength of illumination (λ) expressed as

$$\mu = \frac{4\pi\beta}{\lambda} \tag{2.3}$$

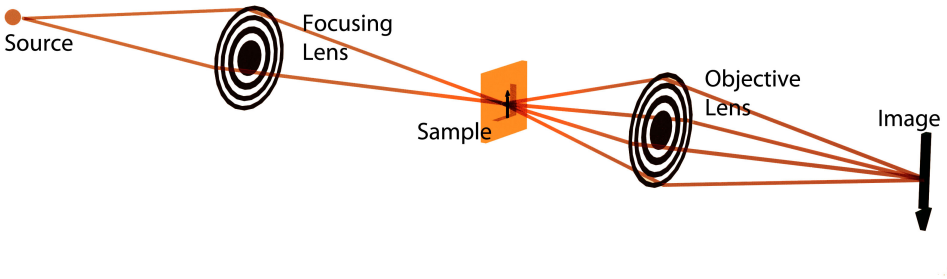

Figure 2.1: Schematic Diagram of a SXR microscope.

Even though absorption is the major contrast mechanism for SXR microscopy, there is generally a non-negligible phase shift ϕ:

$$\phi(t) = \frac{2\pi\delta}{\lambda}t, \tag{2.4}$$

where δ is the real part of the refractive index of the material.

Soft X-ray microscopy has special popularity in the so-called *water window*, between the oxygen and carbon absorption edges (wavelengths 2.3 - 4.4 nm). In this region, the attenuation length $(1/\mu)$ differs strongly between organic compounds and water, and thus provides enhanced natural contrast in the imaging of biological specimens in aqueous environments.

The simplest form of an optical microscope consists of a light source, focusing and imaging lenses, and a detector. In this chapter we consider SXR microscopy using diffractive optics as imaging lenses. Prior to further dicussion, we will review the existing SXR sources, available optics, and assess the characterization and performance of SXR imaging systems.

2.1 Soft X-ray Sources

Generating SXR radiation for practical applications is not trivial. Prior to describing the main different approaches to create SXR radiation, let us define the parameter most commonly used for comparative purposes: brightness.

Light sources are typically compared by the **spectral radiance** $[W/(sr \times m^2 \times BW)]$, that is, a measure of the average energy per unit time per unit area per unit solid angle divided by the bandwidth. The bandwidth normalization is unanimously agreed across the synchrotron radiation community to be of 0.1%, although different communities within the X-ray field develop their own units and terminologies depending on the source. Instead, **spectral brightness** is often used. For spectral brightness [Photons/$(s \times sr \times m^2 \times BW)$], the power of the radiation is often omitted by quantifying the number of photons created by the SXR source at a given line within a bandwidth relative to the energy of that line.

There exist a multitude of SXR sources today. These sources can be classified in three different categories: synchrotron sources, free-electron lasers (FELs), and compact sources. A brightness comparison chart of some X-ray sources is shown in figure 2.1, which includes the aforementioned groups. Generally, high-resolution SXR microscopy requires monochromatic high-brightness sources, preferably tunable in wavelength and coherence. Following these criteria, synchrotron radiation has until very recently been the best choice for imaging, although great progress of table-top and high-harmonic sources has increasingly shown very interesting properties for SXR microscopy. Moreover, FELs have recently introduced a revolutionary merge of ultrashort pulse duration and peak spectral brightness. Here, we summarize the most relevant sources for SXR microscopy with nanoscale resolution.

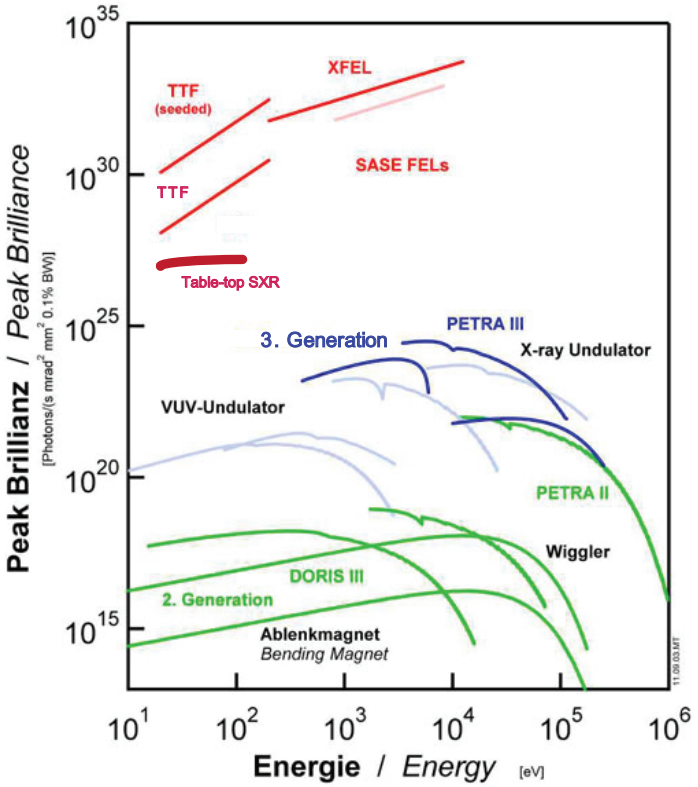

Figure 2.2: **Peak Spectral Brightness Comparison Chart:** Peak brilliance of X-ray FELs and undulators for spontaneous radiation in comparison with synchrotron radiation sources. Brilliance is expressed as photons/$(s \cdot mrad^2 \cdot mm^2)$ per 0.1% BW [87].

2.1.1 Synchrotron Radiation

It is well known that a charged particle will emit electromagnetic radiation when accelerated or decelerated. Synchrotron radiation is generated by relativistic electrons undergoing a change in direction, thus acceleration, in a storage ring, where electrons are maintained at a constant kinetic energy on the order of 10^9 eV.

When an electron beam is bent a broadband energy spectrum of photons is emitted. The spectrum usually covers from infrared to soft X-rays [20].

There are three principal methods for generating synchrotron radiation: bending magnets, undulators and wigglers [88, 20]. Wigglers and undulators, called insertion devices, are placed in the straight sections between the bending magnets.

They can produce narrower photon energy spectrum. The periodic nature of these magnetic structures shape the electron oscillations dependent on the magnetic field strength and a dimensionless parameter called *magnetic deflection parameter* and defined as $K = \frac{eB_0\lambda_u}{2\pi mc}$, where B_0 is the periodic magnetic field amplitude and λ_u is the period of the magnetic structure.

When $K < 1$ the insertion device is called an **undulator** and the source is characterized by a wavelength-tunable, partially coherent, narrow bandwidth and high spectral brightness beam. When $K >> 1$, the strong magnets makes the oscillation of the electron beam larger and non-sinusoidal. This insertion device is called **wiggler**. A direct consequence of a large K is a strong generation of harmonics, which merge into a continuum for higher photon energies. The photon flux and energies are much larger in wigglers than in bending magnets or undulators.

Undulators and wigglers are very commonly used in combination with monochromators in order to exploit very narrow bandwidths for the illumination of microscopy applications. In terms of repetition-rate, since the electrons travel in bunches in the storage ring, the photon flux is not continuous, although light pulses with duration $> 200ps$ separated $10^{-10} - 10^{-11}$ seconds are typically extracted. Arbitrarily polarized undulator radiation can be generated by using specialized magnet structures and K-values, which is of great interest for applications with polarization dependent properties, such as probing magnetic materials and helical structures.

2.1.2 Free Electron Lasers

The operating principle of the free-electron laser (FEL) has many similarities with synchrotron sources. In a FEL the active medium consists of a beam of free electrons traveling at relativistic velocities in an undulator, where the electrons follow transverse oscillations and emit radiation in the forward direction. For this reason, both the *magnetic deflection parameter* - K and the *relativistic factor* -

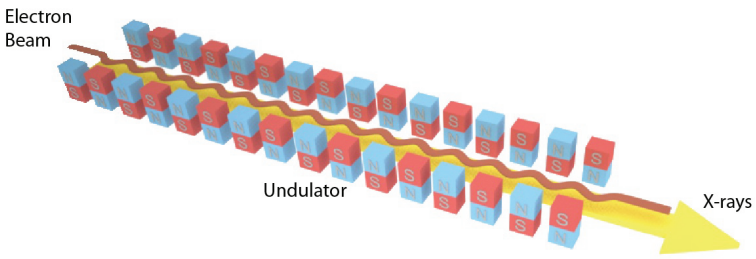

Figure 2.3: Principle of operation of a FEL

γ are completely analogous to what has been discussed in the previous section. Obviously, FELs exhibit free tunability of the wavelength by changing either the electric E or magnetic B field. The fundamental wavelength of the FEL radiation is related to the period of a planar undulator λ_u by

$$\lambda = \frac{\lambda_u}{2\gamma^2}\left(1 + \frac{K^2}{2}\right) \tag{2.5}$$

Presently, SASE FELs have demonstrated revolutionary light attributes reaching the X-ray region surpassing by several orders of magnitude third-generation synchrotron spectral brightness and featuring wavelengths as low as a few Å $10^{11} - 10^{12}$ photons per pulse, and femtosecond pulse durations, although not simultaneously [89, 90]. These sources are still under intense development towards shorter wavelengths and higher average power.

2.1.3 Compact sources

Compact SXR sources capable of producing high average powers can make accessible a wide variety of new studies in science and enable the development of unique metrology and processing tools for industry. This section aims to review the most relevant compact SXR sources.

Laser-produced Plasmas

The laser-produced plasma (LPP) source is one of the alternatives to synchrotron sources only for very specific applications. In a LPP a hot dense plasma is formed in a small volume when a high peak-power laser pulse is focused onto a target material. Initially, during the first picoseconds of the laser pulse free electrons are created. The plasma is then rapidly heated by energy transfer from the incoming photons to the kinetic energy of free electrons, i.e., inverse bremsstrahlung absorption. As the plasma is heated, more free electrons are generated and an electron density gradient arises. The electron distribution oscillates at a frequency called *plasma frequency* defined as $omega_p = \left(\frac{e^2 n_e}{\epsilon_0 m_e}\right)^{1/2}$, where n_e is the electron density, e is the electron charge, m_e is the electron mass, and ϵ_0 is the vacuum permeability. The propagation of the incoming radiation through the plasma can occur if $\omega > \omega_p$ is satisfied.

Generally, a plasma with ions of low atomic number has nearly or fully ionized atoms and line emission dominates the radiated spectrum. A plasma of higher atomic number ions has a blackbody-shaped spectrum with superposed characteristic line emission predominantly from recombination and bound-bound transitions. Consequently, the emission spectrum from a laser-plasma source can be tuned by varying the target material and plasma temperature, but is clearly characterized by a bulb-like, i.e. incoherent, behavior, unless very specific lasing conditions are met [91]. The properties of a laser plasma are determined by a complex relation between laser absorption, electron and ion temperature, density, expansion rate, photon emission and re-absorption, and coupling between acoustic and electromagnetic waves [92].

Discharge-pumped SXR Lasers

Lasing requirements at EUV and SXR wavelengths can be met through the use of z-pinch capillary discharges, firstly observed by Rocca et al. in 1994 [93, 94].

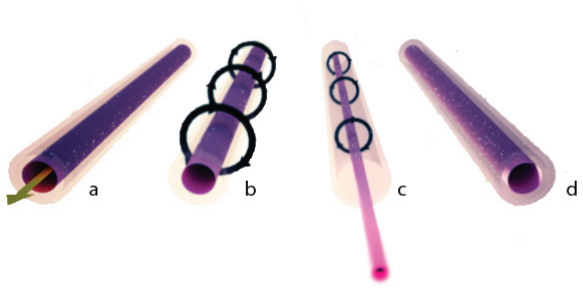

Figure 2.4: **Z-pinch Dynamics. a,** A capillary with two electrodes at both ends is filled with a gas. A high voltage is applied rapidly and a discharge takes places, flowing current to one electrode to the other. **b,** The Lorentz force created by the fast current compresses the plasma column inwards. **c,** The plasma becomes hotter and denser while compressing. It will continue compressing until the plasma pressure equals the magnetic pressure (z-pinch) where lasing conditions are met. **d,** After this point the hot dense plasma is under expansion.

This approach consists of generating the lasing media by collisional excitation. In this scheme a plasma column is generated by a fast discharge in capillary channels filled with a gas. The Lorentz force created by the fast current pulse rapidly compresses the capillary plasma and forms a dense hot plasma column. The plasma conditions for soft X-ray amplification are met by collisional excitation of multiply ionized atoms.

Fast capillary discharges have been demonstrated to efficiently generate highly uniform plasma columns, a critical requirement to enable lasing conditions. Large soft X-ray amplification has been demonstrated by collisional excitation in Ne-like ions at wavelengths ranging from 46.9 to 60.8 nm. The emissions from these sources have reached ~ 0.1 mJ level featuring pulse durations in the nanosecond range [95, 96]. Although the extension of discharge-pumped lasers to shorter wavelengths using Ni-like ions is clearly of interest for future table-top experiments, optical excitation is used instead for SXR amplification, as discharge excitations schemes face very unfavorable pumping demands for higher photon energies. These alternative approaches will be discussed in the subsequent sections.

The wavelengths covered by this excitation schemes usually lie in the lower end of SXR and EUV photon energies for saturated and large amplifications. To set an example, the 46.9 nm wavelength discharge capillary laser produces pulse of 1.5 ns duration with a repetition rate as high as 10 Hz. Moreover, the spectral brightness is a few orders of magnitude higher than that of the synchrotron sources, typically of $10^{25} photons/(s \times mrad^2 \times mm^2)$ per 0.01 % BW. The radiation emitted is very monochromatic ($\Delta\lambda/\lambda < 10^{-4}$). The plasma density profile in the capillary exhibits an on-axis maximum that results a refraction of the amplified radiation. This refraction is an effective mode-selection mechanism resulting in an increase of the spatial coherence with amplification length. Therefore, for saturated amplification, the spatial coherence of the radiation can be tuned from partially to fully coherent by simply varying the gain medium length [97].

The coherence and short wavelength attributes of discharge capillary lasers have been exploited to demonstrate various techniques of nanoscale imaging, nano-patterning, and metrology [98, 99, 100, 101, 102, 103].

Laser-pumped SXR Lasers

The principle of operation of these lasers is analogous to that of the capillary discharge, where spontaneous emission generated by the plasma or an externally generated coherent seed, is amplified by stimulated emission in a population inversion created between energy levels of plasma ions. These collisional lasers require highly ionized plasmas (8-25 times) to produce amplified emission in the SXR spectral region. These high ionization levels compel the creation of plasmas with very high electron temperatures and densities, typically of 0.3-1 keV and $10^{20} cm^{-3}$, respetively, which are several orders of magnitude higher than those for singly ionized collisional lasers in the visible spectrum. Therefore, the challenge for these table-top plasma-based lasers has been and continues to be the extension of their range of operation to shorter wavelengths and the increase of their peak brightness and average power.

Early significant work was realized at LLNL where gain in plasmas was demonstrated for wavelengths as short as 35.6 Å [104]. During the past few years, several groups have successfully developed laser-pumped SXR lasers with stable output for practical applications and repetition rates reaching up to 10 Hz [105, 106, 107, 108]. Collisional lasing has been demonstrated in both Ne-like and Ni-like ions. As of today, the shortest wavelength achieved in gain-saturated table-top lasers is 10.9 nm by amplification of spontaneous emission in Ni-like tellurium ions in a plasma generated at a 1-Hz repetition rate by the irradiation of a solid tellurium target with pulses from a chirped amplification Ti:Sapphire laser [109]. This laser is capable to output pulses of up to 2 μJ and an average power of 1 μW in the picosecond pulse duration range. Most recently, Rocca et al. have reached 10 μJ pulse energies through a similar setup on a table-top generated by a Ni-like Ag SXR laser at 13.9 nm [110]. This laser is operated at 2.5 Hz, resulting in 20 μW average power.

The most common laser drivers used are high-energy Ti:Sapphire lasers and Nd:glass pump lasers, which feature typical repetition rates of 10 Hz. For this

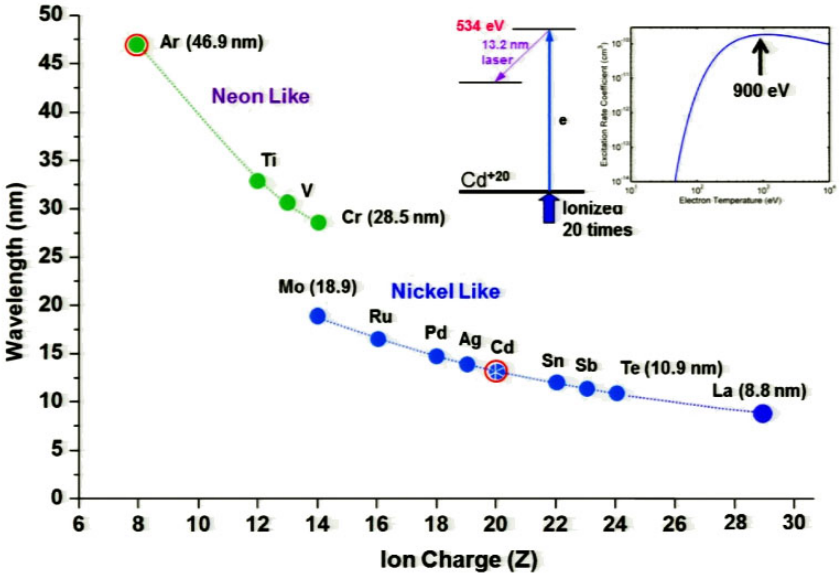

Figure 2.5: **Collisional Laser Demonstrations** of SXR table-top lasers. Ni-like ions (blue) provide access to shorter wavelengths (Ne-like ions in green).

reason, diode-pumped solid-state lasers are currently being developed [111, 112] in order to greatly increase their repetition rate (hence, average power) by at least an order of magnitude (> 100 Hz). Ongoing progress has also been achieved in improving the beam characteristics of plasma-based SXR lasers. Injection-seeding of SXR laser amplifiers with high harmonic pulses have been shown to generate intense fully phase coherent SXR pulses with lower divergence, shorter pulse-width, and defined polarization [113]. This approach generates significantly denser plasmas by heating solid targets that can support the amplification of femtosecond pulses [114, 115]. Moreover, the pulse duration in a self-seeded SXR laser is determined by the duration of the gain. The recent demonstration of injection-seeding with high harmonics brings a different scenario where the pulsewidth is governed by the amplifier bandwidth and is independent of the gain duration. Injection-seeded plasma amplifiers are expected to result in femtosecond SXR laser pulses, extending the applications for these table-top lasers to ultrafast dynamic studies.

High-harmonic Generation

Another approach towards SXR radiation is through the generation of high harmonics using high-intensity ultrashort laser pulses in gaseous media. The strong nonlinear interactions between the electric field from the laser and the gas that are responsible for the upconversion of the laser. Typically, the laser intensity has to surpass $10^{14} W/cm^2$ and feature pulse lengths of the order of a few tens of femtoseconds. High-harmonic generation is thus far the only available method capable of producing attosecond ($10^{-18} s$) pulses in the SXR and X-ray regions [116, 117].

The harmonic generation process can be described microscopically by a three-step semiclassical recollision model [119]. First, an electron tunnels out of the Coulomb potential barrier suppressed by the laser field and moves away from the ion. Once liberated, the electron is strongly accelerated by the field. When the

oscillating laser field is reverted the electron is driven back and it violently collides with its parent ion. Any kinetic energy excess during this recombination process is emitted as a higher energy (upconverted) photon. A typical high-order harmonic spectrum shows that with the increase of harmonic order, the signal intensity falls off drastically for the first few low orders. However, after the intensities remain almost constant for many orders (the *plateau*), the intensity finally drops abruptly for the highest orders, the so-called single-atom cutoff, expressed as

$$h\nu_{cutoff} = E_{cutoff} = I_p + 3.17U_p, \tag{2.6}$$

where I_p is the ionization potential of the atom and U_p is the average kinetic energy of a free electron oscillating in the laser field, defined as

$$U_p(eV) = 9.33 \times 10^{-14} I_L \lambda_L^2, \tag{2.7}$$

where $I_L(Wcm^{-2})$ and $\lambda_L(\mu m)$ are the pump laser intensity and wavelength, respectively. The radiation produced is spatially coherent and has a small divergence angle. Most atoms emit harmonics over a broad range of photon energies. However, in order to produce a bright output beam the emission of a large num-

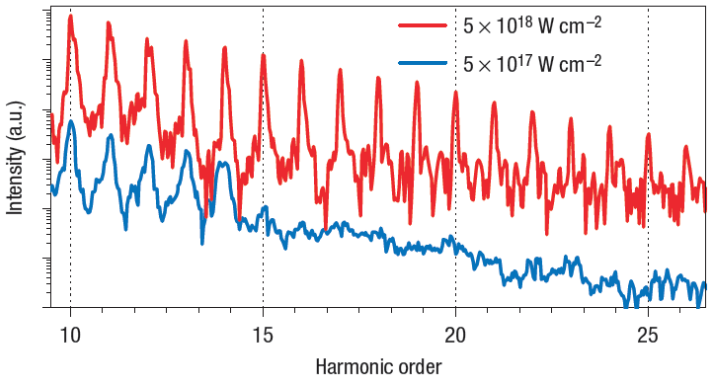

Figure 2.6: **Representative HH Spectrum:** simulated harmonic spectra for two different laser intensities and a fixed plasma density [118].

ber of atoms must add in phase, condition that is satisfied when the drive laser and the generated X-rays travel at the same velocity in the nonlinear medium, called *phase-matching* [120, 121]. For relatively low photon energies (< 100 eV) phase-matching is readily met, enabling photon energy conversions over centimeter lengths which lead to μW coherent beams in the EUV region [122, 123]. From the expressions above, it is clear that higher photon energies (> 100 eV) require higher laser intensities, which strongly ionize the gas medium. Highly ionized media increase the dispersion of the drive laser in the plasma and hence induce a phase slip relative to the generated harmonic field. Therefore, coherent addition of the emitted fields is only possible over very short distances in the medium. In the absence of phase matching, the harmonic emission builds up periodically over a coherence length and then interferes with out-of-phase light generated in the next section of the nonlinear medium, drastically reducing the total flux. In the SXR region HHG can be efficiently realized through a phase corrective scheme called *quasi-phase-matching* proposed by Armstrong et al. [124], whereby the phase mismatch is periodically corrected by introducing a periodicity to the nonlinearity of the medium equal to the coherence length. To date, quasi-phase-matching has been successfully performed for photon energies up to 330 eV [125].

2.2 Soft X-ray Optics

Microscopy involves focusing and redirecting of the radiation using optical components. The conditions under which soft X-ray radiation can be manipulated relative to conventional microscope schemes, though, are quite different to those in the visible range. The refractive index in the SXR region exhibits very strong resonances. The extinction coefficient (the imaginary part of the refractive index) is large, which is why diffraction and reflection lenses are used instead of refractive lenses.

The optical response of materials to soft X-ray radiation is governed by the same classical equations for all electromagnetic radiation [20]. However, the response can outcome very differently because the real part of the complex refractive index in the SXR region is very close to one, for example, *total external reflection* instead of *total internal reflection*. A plane wave propagating in some material is given by

$$\mathbf{E}(\mathbf{r},t) = \mathbf{E}_0 e^{-i(\omega t - \mathbf{kr})}, \tag{2.8}$$

where the complex propagating vector $\mathbf{k}$ is

$$k = \frac{\omega}{c} n = \frac{\omega}{c}\left(1 - \delta - i\beta\right) \tag{2.9}$$

For X-rays, the refractive index is usually expressed as $n = 1 - \delta - i\beta$. Both parameters are related to the complex atomic scattering factor $f^0 = f_1^0 - i f_2^0$ by

$$\delta = \frac{n_a r_e \lambda^2}{2\pi} f_1^0\left(\omega\right), \tag{2.10}$$

$$\beta = \frac{n_a r_e \lambda^2}{2\pi} f_2^0\left(\omega\right), \tag{2.11}$$

where n_a is the atom density and r_e is the classical electron radius. There are various analytical models to estimate both values f_1^0 and f_2^0, although values tabulated by Henke et al. are a commonly applied [126]. By substituting n in equation 2.8 we obtain

$$\mathbf{E}(\mathbf{r},t) = \mathbf{E}_0 e^{-i\omega(t - r/c)} e^{-i(2\pi\delta/\lambda)} e^{-(2\pi\beta/\lambda)} \tag{2.12}$$

where the first exponential represents the phase advance through vacuum, the second represents the phase-shift due to the medium, and the third represents the absorption.

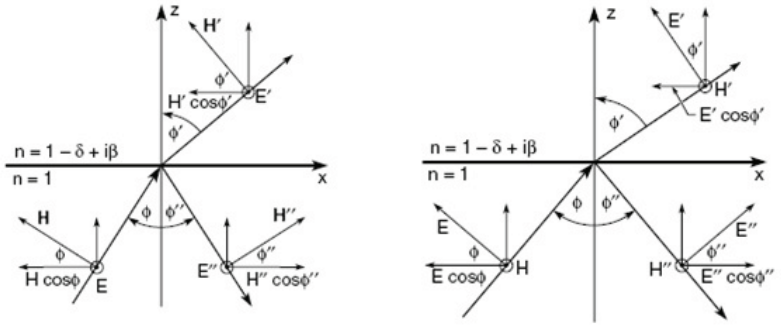

Figure 2.7: *s-* and *p-polarized* incident, reflected and refracted waves at the interface of two media [20].

We will consider the role of δ and β shaping the optical response of SXR radiation next. This section is dedicated to a brief description of the principles of reflective and diffractive optics, with special emphasis in Fresnel zone plates.

2.2.1 Fresnel Equations in the SXR Region

The reflection and transmission coefficients of electromagnetic waves is governed by boundary conditions for the electric E and magnetic H fields at the interface between two different media, shown in figure 2.7. From these relationships, the reflectivity R at an interface is expressed as the ratio between the reflected and the incident intensities determined by

$$R = \frac{\overrightarrow{I_0''}}{\overrightarrow{I_0}} = \frac{Re\left(E_0'' \times \{H_0''^*\}\right)}{Re\left(E_0 \times H_0^*\right)} \tag{2.13}$$

Then, the reflectivity for *s-* and *p-polarization* is shown in the Fresnel equations as

$$R_s = \{\frac{|n_1 cos\phi - n_2 cos\phi^{'}|}{|n_1 cos\phi + n_2 cos\phi^{'}|}\}^2 \tag{2.14}$$

$$R_p = \{\frac{|n_2 cos\phi - n_1 cos\phi^{'}|}{|n_2 cos\phi + n_1 cos\phi^{'}|}\}^2 \tag{2.15}$$

For soft X-rays, δ is small and positive for most materials, that is, the real part of the refractive index is slightly less than unity, which results in overall low reflectivity except for grazing angles. At normal incidence the reflectivity is almost negligible, which presents important implications for the design of multilayer interference coatings.

2.2.2 Multilayer Mirrors

Multilayer coatings greatly increase the reflectivity in EUV and SXR regions. Even at grazing incidence, these mirror exhibit several advantages over monolayer mirrors, such as smaller aberrations or larger collection efficiency [128]. Most generally, these coatings consist of two alternating materials with low and high Z so that the difference in refractive index is maximized. Presently, much is being invested in the development of Mo/Si multilayer-coated mirrors for extreme ultraviolet lithography (EUVL) at 13.5 nm with a reflectivity of 72% at normal incidence [129].

Multilayer mirrors obey Bragg's law and hence have limited spectral bandwidth. Scattering of electromagnetic radiation occurs at locations where the refractive index varies. The idea behind multilayer structures is that the thickness of each layer is chosen so that scattered radiation interferes constructively. Since energy and

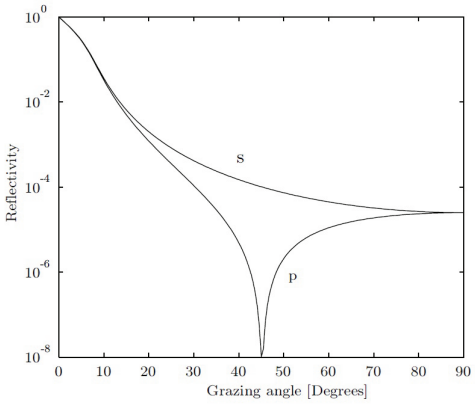

Figure 2.8: **Reflectivity Curves** for *s-* and *p-polarization* X-ray incident on a gold monolayer calculated with IMD [127].

momentum is conserved in the scattering process, the energy ($\hbar\omega$) and momentum $\hbar\mathbf{k}$ of the incident (i) and scattered (s) waves are related to the *stationary charge density distribution wave* (d) as follows

$$\hbar\omega_s = \hbar\omega_i + \hbar\omega_d, \tag{2.16}$$

$$\hbar\mathbf{k}_s = \hbar\mathbf{k}_i + \hbar\mathbf{k}_d, \tag{2.17}$$

where $\hbar\omega_d$ and $\hbar\mathbf{k}_d$ are a mathematical representation of the energy and momentum of the multilayer structure. Since the multilayer density distribution does not vary $\omega_d = 0$, hence $\omega_s = \omega_i$, resulting in

$$|\mathbf{k}_s| = |\mathbf{k}_i| \tag{2.18}$$

Simplifying the multilayer structure wave as a sinusoid, the general form of Bragg's law can be derived

$$m\lambda = 2dsin\theta, \tag{2.19}$$

where d is the multilayer period, λ is the wavelength, θ the grazing angle and $m = 1, 2, 3, ...$ From the simplest form of Bragg's law it can derived that there only exists one possible value for the multilayer period for constructive interference, given a wavelength and a single angle of incidence. In reality, the multilayer structures acts as a band-pass filter, where the spectral bandwidth of roughly

$$\frac{\lambda}{\Delta\lambda} \approx mN, \tag{2.20}$$

and N is the number of pair layers. There are several available advanced models

that calculate optical properties of multilayers for most relevant materials, wavelengths, and incident angles that consider interlayer roughness, intermixing and non-periodical structures for novel designs of multilayer coatings [127, 129]. Several application-specific multilayer mirrors have been developed to cover the EUV and SXR spectrum. For larger wavelengths, from 25 to 50 nm, Sc/Si and Mg/SiC multilayers are often fabricated with typical normal incidence efficiencies of 30-60 % [130, 131]. Moreover, tri-material multilayer coatings, such as Co/Mg/B_4C and Mg/Sc/SiC, have also been demonstrated in this longer wavelength range for increased reflectivity and bandwidth tunability [132, 133]. For shorter wavelengths, from 15 nm to 1 nm, Si/Mo, Y/Mo, La/B_4C, Cr/Ss, and W/B_4C have been fabricated and studied in depth [134]. Novel multilayer coating designs have also been demonstrated for ultrafast pulses [135, 136].

2.2.3 Diffractive Optics

Diffractive opctical elements are most commonly used in the SXR region, which primarily consist of linear gratings and focusing Fresnel zone plates. The former are often used as monochromators or spectrographs. Their ability to deviate electromagnetic radiation is governed by Bragg's law form of the transmission grating formula at arbitrary incidence

$$d\,(sin\alpha + sin\theta) = m\lambda, \tag{2.21}$$

where d is the period of the grating, α is the angle of incidence and θ is the angle of deviation. The resolving power limited by its bandwidth (as in equation 2.20).

For a transmission grating consisting of opaque lines of width equal to half the grating period, the diffraction efficiency η_m is given by

$$\eta_m = \begin{cases} 0.25 & m = 0 \\ 1/\mathrm{m}^2\pi^2 & m \text{ odd} \\ 0 & m \text{ even} \end{cases} \tag{2.22}$$

The diffraction efficiency of the gratings in limited to 10% in the first order. However, the efficiency can be greatly improved if the "opaque" lines are replaced by a translucent phase-shifting material. Ideally, this material should give a π phase-shift and no absorption, which increases its efficiency to a 40% in the first order. Most generally, a compromise between phase-shift and absorption must be made. The theoretical diffraction efficiency of a general grating (this includes Fresnel zone plates) with absorption and phase shift included for any non-zero order is given by,

$$\eta_m = \frac{sin^2(rm\pi)}{(m\pi)^2}\left[1 + e^{-4\pi\beta t/\lambda} - 2e^{-2\pi\beta t/\lambda}cos(2\pi\delta t/\lambda)\right], \tag{2.23}$$

where r is the line-to-space ratio and t is the thickness of the lines. The choice of the material is not trivial, since other factors, such as long-term stability and fabrication aspects, must be taken into account. Most frequently Au, Ge and Ni are used for soft X-rays [137].

In the soft X-ray regime, zone plates have become a standard focusing component for high resolution imaging. They offer practically aberration free performance at a moderate cost compared to other compound focusing reflective optics. These circular gratings with radially decreasing periods perform point-to-point imaging, just like conventional lenses. Zone plates have the highest resolving power among all focusing elements. On the other hand, they feature multiple diffraction order and strong zero order background, which for the aforementioned reasons ultimately limits their efficiency to $10 - 40\%$. The following section is dedicated to a brief description of amplitude Fresnel zone plates.

2.2.4 Fresnel Zone Plates

In general terms, a zone plate consists of a set of concentric circular opaque-transmission patterns that focus light by exploiting diffraction through circular transmission gratings. Owing to diffraction, radiation is redirected in a new given direction near sharp edges.

The zonal radii r_n are related to the focal length of the lens f by the Pythagorean Theorem by

$$f^2 + r_n^2 = \left(f + \frac{n\lambda}{2}\right)^2, \tag{2.24}$$

where $n\lambda/2$ defines the incremental path length to the focal point. Thus, the radii are given by

$$r_n^2 = n\lambda f + \frac{n^2\lambda^2}{4} \tag{2.25}$$

Assuming that $f \gg n\lambda/2$, i.e., provided a small numerical aperture $NA = sin\theta = \lambda/(2\Delta r) \ll 1$, where Δr is the outermost zone width, the term $n^2\lambda^2/4$, which represents the spherical aberration of the lens, can be neglected. Under this assumption,

$$r_n^2 \simeq \sqrt{n\lambda f} \tag{2.26}$$

Clearly, one of the most influential zone plate parameters in the outer zone width Δr, which shapes the NA of the lens, hence, determines the best achievable resolution for a given wavelength. The spatial resolution is limited by this factor as follows. By definition,

$$\Delta r = r_N - r_{N-1}, \tag{2.27}$$

where N is the total number of zones. By introducing the approximation in equation 2.26

$$r_N^2 - r_{N-1}^2 = N\lambda f - (N-1)\,\lambda f = \lambda f \tag{2.28}$$

$$r_N^2 - (r_N - \Delta r)^2 = 2r_N\Delta r - (\Delta r)^2 \simeq 2r_N\Delta r \tag{2.29}$$

Thus,

$$\lambda f \simeq 2r_N\Delta r, \tag{2.30}$$

or

$$\lambda f \simeq D\Delta r, \tag{2.31}$$

where $D = 2r_N$ is the total lens diameter. Using this expression in equation 2.26

$$D \simeq 4N\Delta r \tag{2.32}$$

The focal length of the lens can then be expressed as

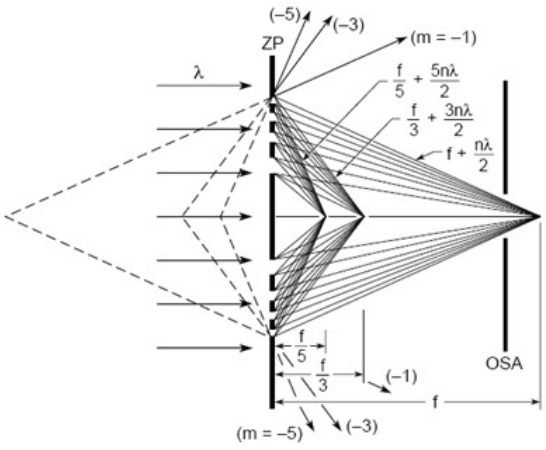

Figure 2.9: Zone plate diffractive focusing for higher order [20].

$$f \simeq 4N\frac{(\Delta r)^2}{\lambda} \tag{2.33}$$

There are several conclusions that can be derived from these expressions. First and foremost, zone plate lenses are strongly wavelength dependent. In order to prevent strong chromatic aberration, the spectral bandwidth of the illumination is required to be extremely narrow ($\Delta\lambda \leq 1/N$). For any lens, the numerical aperture is defined by

$$NA = sin\theta = \frac{r_N}{f} = \frac{D}{2f}, \tag{2.34}$$

or alternatively for zone plate lenses

$$NA \simeq \frac{\lambda}{2\Delta r} \tag{2.35}$$

According to the Rayleigh resolution criterion given by the radius of the first null of the Airy pattern, the best achievable spatial resolution is given by

$$res = \frac{0.61\lambda}{NA}, \tag{2.36}$$

or

$$res = 1.22\Delta r \tag{2.37}$$

The *depth of field*(DOF) of a lens provides a quality factor of its performance by determining the admissible axial displacement away from the focus plane which causes an acceptable degradation of either the intensity or the image resolution. The most widely acceptable criterion determines the displacement from the ideal focal plane where the on-axis intensity decreases by 20% from the highest axial intensity at $z = f$ as

$$\Delta z = \pm \frac{1}{2} \frac{\lambda}{(NA)^2} = \pm \frac{2(\Delta r)^2}{\lambda} \tag{2.38}$$

The expression above shows a NA^{-2} dependence of the DOF. As higher NA values will enhance the resolution of the imaging system, these may also lead to nanoscale values of the DOF. Such small values of the DOF create extremely critical imaging conditions as astigmatic aberrations may begin to play a decisive role.

2.3 The Generalized Imaging System

Conventionally, the spatial resolution (δ) of any imaging system is expressed as $\delta = k\lambda/NA$. In order to understand the limiting factors of microscopy, some fundamental principles of image formation are presented in this section. There are critical factors that impact the formation and quality of an image, such as the coherence, properties of the illumination (e.g. chromaticity or wavelength), the depth of field or the object itself, among others. Let us discuss some of these main attributes.

2.3.1 Spatial and Temporal Coherence of the Source

A well defined coherent radiation sets angular limits on diffraction and enables the recording of interference patterns.

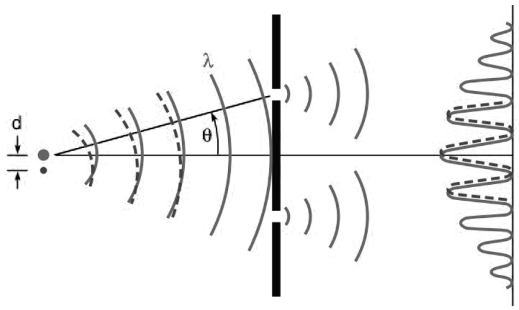

Figure 2.10: Representation of interference fringes created from a point source.

In the quasi-monochromatic approximation (long coherence length l_{coh}), an object composed of two point sources interfere with a contrast mechanism proportional to their mutual coherence

$$\mu = \frac{\langle E_1(t) E_2^*(t) \rangle}{\sqrt{\langle |E_1|^2 \rangle} \sqrt{\langle |E_2|^2 \rangle}}, \tag{2.39}$$

where μ is the *complex coherence factor*, which acts as a normalized degree of spatial coherence. A high degree of coherence ($\mu \to 1$) implies an ability to form a high contrast interference, while a low degree of coherence ($\mu \to 0$) implies an absence of interference.

The spectral bandwidth is tightly related to the longitudinal (temporal) coherence, characterized by the *coherence length*, defined as the distance of propagation over which radiation of spectral width $\Delta\lambda$ becomes $\pi/2$ out of phase. For a wavelength λ propagating through N cycles

$$l_{coh} = N\lambda, \tag{2.40}$$

and for a wavelength $\lambda + \Delta\lambda$, a half cycle less $(N - 1/2)$

$$l_{coh} = \left(N - \frac{1}{2}\right)(\lambda + \Delta\lambda) \tag{2.41}$$

Equating both

$$N = \frac{\lambda}{2\Delta\lambda}, \tag{2.42}$$

so that

$$l_{coh} = \frac{\lambda^2}{2\Delta\lambda} \tag{2.43}$$

2.3.2 Coherence of the Imaging System

Transverse (spatial) coherence refers to phase correlation in planes orthogonal to the propagation. Conceptually, it can be understood as a set of concentric spherical waves perfectly correlated everywhere within a well-defined direction. From Heisenberg's Uncertainty Principle $\left(\Delta x \Delta p \geq \frac{\hbar}{2}\right)$, the smallest source size d one can resolve with wavelength λ and half-angle θ is called *diffraction limit* and expressed as $d \cdot \theta = \lambda/2\pi$, equality that serves as a good estimate to generate spatially coherent spherical waves. A bright-field microscope behaves as a partially coherent system in which the coherence parameter σ is given by the ratio of the numerical apertures of the illuminating wave, typically from a condenser, and the objective as

$$\sigma = \frac{NA_{con}}{NA_{obj}} = \frac{n_{con} sin(\theta_{con})}{n_{obj} sin(\theta_{obj})}, \tag{2.44}$$

where θ_{con} and θ_{obj} are the aperture angles of the condenser and objective lens, respectively, and n_{con} and n_{obj} are the corresponding indices of refraction. If $\sigma = 0$, not to be confused with μ, the optical system behaves coherently, while if $\sigma \geq 1$ it behaves incoherently. Generally, imaging systems are partially coherent $(0 < \sigma < 1)$.

2.3.3 The Generalized Pupil Function

We begin with the assumption that an imaging system creates a real-space image by representing the properties of the lens by an entrance and exit pupil adequately described by geometrical optics. In a diffraction-limited imaging system, the point-spread function (PSF) is the Fraunhofer diffraction pattern of the exit pupil and centered on the ideal image point. Any aberrations present in the system can be represented by waveform deformation of a perfect illuminating spherical wave at the pupil exit. The *effective path-length error*, $kW(x, y)$, represents the phase

error in the wavefront and gives a *generalized pupil function* $\mathbf{P(x,y)}$ as

$$\mathbf{P(x,y)} = P(x,y)exp[jkW(x,y)] \tag{2.45}$$

The generalized pupil function refers to the complex amplitude transmittance. It is demonstrated that the PSF of an aberrated partially coherent system is simply the far-field diffraction pattern of an aperture with amplitude $\boldsymbol{P}$ [138], as in equation 2.45. Thus, if a system is free of any form of aberration, the exit pupil is filled by a perfect spherical wave.

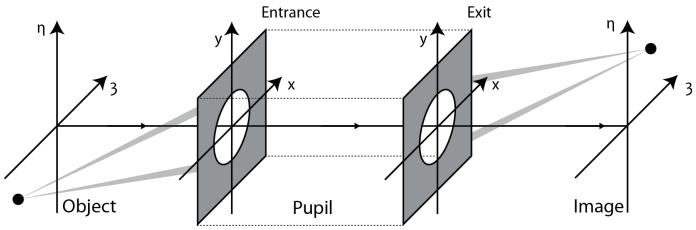

Figure 2.11: Generalized Imaging System

Focusing-error is the simplest form of aberration in diffraction-limited optical systems. Let us assume a perfect spherical wavefront at a square aperture of width $2w$. When a focusing error is present, the center of curvature of the spherical wavefront converging towards the image place lies either prior to or after the image plane. The phase distribution at the exit pupil is of the form

$$\phi(x,y) = -\frac{\pi}{\lambda z_a}\left(x^2+y^2\right), \tag{2.46}$$

where $z_a \neq z_i$. The path-length error can be determined by subtracting the ideal phase distribution from the actual phase distribution,

$$kW(x,y) = \frac{\pi}{\lambda z_i}\left(x^2+y^2\right) - \frac{\pi}{\lambda z_a}\left(x^2+y^2\right), \tag{2.47}$$

or alternatively,

$$W(x,y) = -\frac{1}{2}\left(\frac{1}{z_a} - \frac{1}{z_i}\right)\left(x^2 + y^2\right) \tag{2.48}$$

We define W_m for the square aperture as an indicator of the severity of focusing error as

$$W_m = -\frac{1}{2}\left(\frac{1}{z_a} - \frac{1}{z_i}\right) w^2, \tag{2.49}$$

which represents the maximum path-length error at the edge of the aperture along the x and y axes. Using this definition

$$W(x,y) = W_m \frac{x^2 + y^2}{w^2} \tag{2.50}$$

This expression can be substituted in a generalized form of the optical transfer function (OTF) that yields

$$\begin{aligned} OTF(f_X, f_Y) = \; & \Lambda\left(\frac{f_X}{2f_0}\right)\Lambda\left(\frac{f_Y}{2f_0}\right) sinc\left[\frac{8W_m}{\lambda}\left(\frac{f_X}{2f_0}\right)\left(1 - \frac{|f_X|}{2f_0}\right)\right] \\ & sinc\left[\frac{8W_m}{\lambda}\left(\frac{f_Y}{2f_0}\right)\left(1 - \frac{|f_Y|}{2f_0}\right)\right] \end{aligned} \tag{2.51}$$

Under this formulae, notice that a diffraction-limited system is obtained when $W_m = 0$. Additionally, for values of W_m greater than $\lambda/2$ the sign reverses. As the system is defocused the contrast attenuates gradually. When the focusing error is severe ($W_m >> \lambda$) the frequency response drops to zero very quickly.

2.3.4 Frequency Spectrum of the Image Intensity

The *Frequency Spectrum* constitutes a simple attribute of an image to compare the effect of coherence. The intensity of incoherent systems follows a linear be-

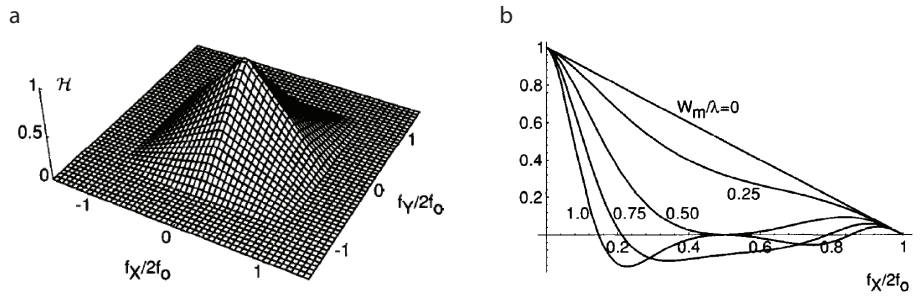

Figure 2.12: **Optical Transfer Function. a,** The normalized optical transfer function of a diffraction-limited system with a square pupil and **b,** f_X cross section of the optical transfer function with W_m/λ as a variable [138].

havior, while coherent systems are highly nonlinear in that quantity (only linear in amplitude). The frequency spectrum of the image intensity distribution for the case of an incoherent imaging system is expressed as

$$FI_{incoh} = [H * H][G * G] \tag{2.52}$$

while for the coherent case it is described by

$$FI_{coh} = [HG] * [HG] \tag{2.53}$$

where

$$X(f_X, f_y) * X(f_X, f_y) = \int\int X(p, q)X^*(p - f_X, q - f_Y)dpdq \tag{2.54}$$

is the autocorrelation integral, H is the amplitude transfer function (magnitude of the OTF) and G is the spectrum of the ideal image U in magnitude and phase [138].

These expressions uncover that frequential content in both cases differs significantly. Furthermore, it shows that the results of a case comparison will strongly depend on both the intensity and phase distributions across the object. For this reason, this general result does not lead to the conclusion that one type of illumination is better than the other in terms of image frequency content, but rather that one object can be said to be imaged better in one case or the other, depending on intensity and phase properties. Because of the lack of a trustful representation of the object and the OTF of a system, this comparison is generally very complex.

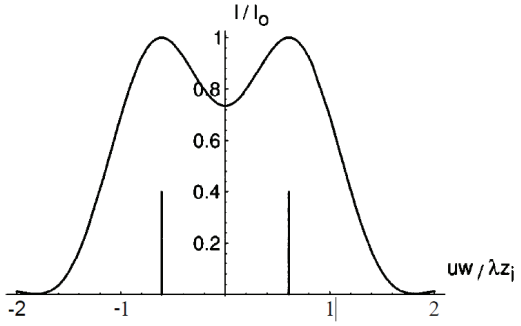

Figure 2.13: **Two incoherent point sources:** Image intensity for two equally bright incoherent point sources separated the Rayleigh resolution distance. The resulting modulation is of 26.5 %. The two vertical lines represent the two incoherent point sources.

2.3.5 Two-point Resolution

According to the *Rayleigh criterion* of resolution, two incoherent point sources are resolved at the limit when the center of the Airy pattern generated by one point source falls exactly on the first zero of the Airy pattern generated by the second. The minimum resolvable separation of the geometrical images is therefore

$$\delta = 0.61\frac{\lambda}{sin\theta} = 0.61\frac{\lambda}{NA} \tag{2.55}$$

where θ represents the half-angle from the exit of the pupil and the NA is the numerical aperture of the optical system. Now, for coherent systems the problem

is found to be more complex and it is found that it also depends on the phase distribution of the object. Let us take a cross-section of the Airy pattern intensity for the most general case where ϕ is the phase between two point sources and write it as

$$I(x) = |2\frac{J_1[\pi(x-0.61)]}{\pi(x-0.61)} + 2e^{j\phi}\frac{J_1[\pi(x+0.61)]}{\pi(x+0.61)}|^2 \tag{2.56}$$

Figure 2.14 shows the distributions of image intensity for point sources with $\phi = 0$ rad, $\phi = \pi/2$ rad, and $\phi = \pi$ rad. When the sources are in quadrature ($\phi = \pi/2$), the image intensity distribution is identical to that resulting from incoherent point sources. When they are in phase ($\phi = 0$), nonetheless, the dip in the image intensity is absent, and therefore the two points are not as resolved as in the incoherent case. Finally, when the two point sources are in phase opposition (($\phi = \pi$)) the dip is of 100% modulation so it can be said that they are better resolved than in the incoherent case. Again, no type of illumination is unambiguously better than the other following this criterion.

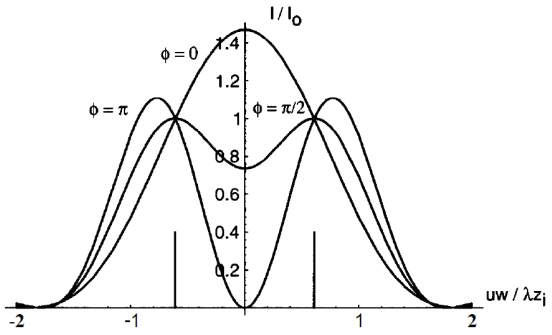

Figure 2.14: **Two coherent point sources:** Image intensities of two equally bright coherent point sources separated by the Rayleigh resolution distance for different phase shifts [138].

2.3.6 Knife-Edge Resolution

There are other common resolution test that bring out properties of images formed with coherent and incoherent light that are notably different. The knife-

edge test relies on the response of an optical system to a sharp edge, or mathematically, a 2D-object with transmittance

$$t_A(x,y) = \begin{cases} 0 & x < 0 \\ 1 & x \geq 0 \end{cases} \tag{2.57}$$

Figure 2.15 depicts some obvious coherent effects in sharp edges. The coherent image crosses the location of the actual edge at $\frac{1}{4}$ of its normalized intensity, where the incoherent image does it at $\frac{1}{2}$ its normalized value. This simple observation is of great relevance when estimating edge positions or widths.

For resolution characterization purposes, the distance over which the normalized image intensity varies from 10% to 90%, d_{10-90} is often used. In principle, d_{10-90} is dependent, as well as δ, on the numerical aperture of the objective lens (NA), the wavelength of illumination (λ), the coherence parameter (σ), and other aberrations in the system. However, d_{10-90} and δ are related as defined only for the incoherent case. For the knife-edge, a higher degree of coherence will provide a sharper edge, hence, better resolution factor, than a lower degree of coherence would.

There are, nonetheless, several coherent artefacts that only arise from the use of coherent illumination. The ripple-effect in sharp edges is highly undesirable as it degrades the overall image quality. Furthermore, coherently illuminated objects

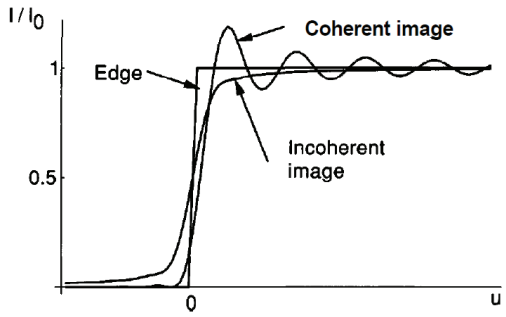

Figure 2.15: **Knife-Edge:** Intensity profile representation of knife-edge images of a sharp perfect edge t_A for the extreme coherent ($\sigma = 0$) and incoherent cases ($\sigma \to \infty$) [138]. Note the intensity normalization.

often display images with a strong granular nature, a direct consequence of the interference between closely spaced and randomly phased scatterers within the diffuser (object), so-called *speckles* [139]. Finally, highly coherent illumination is particularly sensitive to optical imperfections that may exist along a path to the observer. For example, tiny dust particles on a lens may lead to pronounced diffraction patterns superimposed on the image.

Again, it is not straightforward to denote coherent or incoherent imaging undoubtedly better than the other. It seems that partially incoherent illumination would make a good choice in order to avoid the aforementioned effects, although there are techniques that require a high degree of coherence, such as holography or coherent diffractive imaging.

2.3.7 The Grating Test

The grating test describes the modulation response of an imaging system, which can be characterized by analyzing the intensity modulation of a set of periodic objects. These objects are one directional amplitude gratings with an ideal transmission profile varying from zero to one. The intensity modulation the gratings is calculated as $(I_{max} - I_{min})/I_{max}$, that is, the intensity variation $I_{max} - I_{min}$, normalized by the maximum intensity, where I_{min} and I_{max} are the minimum and maximum intensities of the grating image along the propagation axis of the periodic structure, respectively.

Therefore, the modulation response of a microscope denotes the extent of spatial frequencies that are contained in an image. Figure 2.16 represents the effect of coherence on the shape of the modulation response. For perfectly coherent illumination the modulation of decreasing half-period gratings is unity until the half-period reaches a value slightly smaller than Δr, where it abruptly drops to zero (coherent cutoff). As σ begins to increase, the modulation response extends to higher spatial frequencies although with degraded response. The partially co-

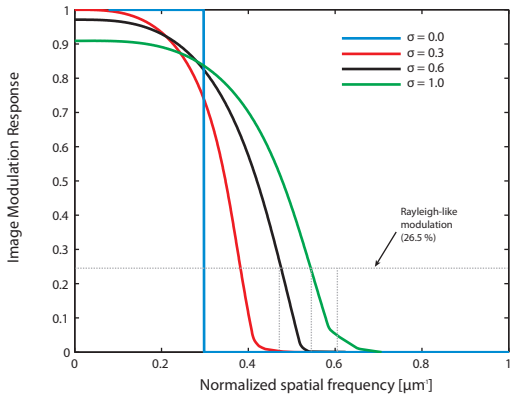

Figure 2.16: **Modulation Response** in varying degrees of coherence to equal line and space patterns

herent cutoff frequency is usually expressed either as Rayleigh-like or zero-drop modulation. For $\sigma = 1$ the modulation is reduced and extends to twice that of the coherent ($\sigma = 0$) case.

2.3.8 Conclusions

In general, no particular value of σ provides optimal image quality for all objects. For an aberration free imaging system, the overall image quality will depend only on the resolving power of the objective lens, the degree of coherence, and the object amplitude and phase distribution. However, the illumination can always

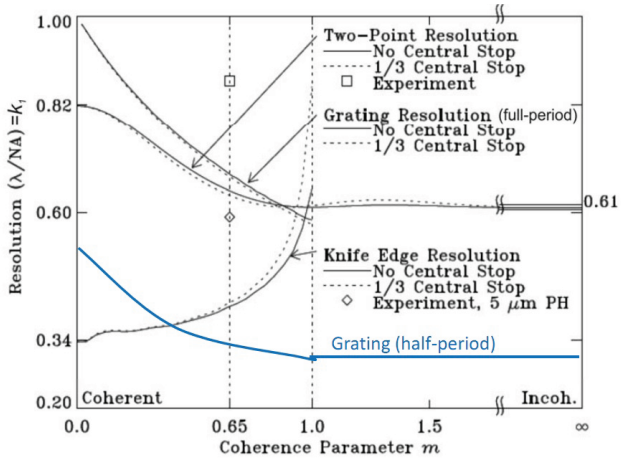

Figure 2.17: Resolution as a function of the degree of coherence as a result of different resolution characterization techniques.

be optimized for specific types of objects. If the imaging technique admits certain coherence flexibility, the best overall imaging performance is typically given by partially coherent illumination.

Unconditionally, none of the resolution criteria discussed in this section constitute an absolute benchmark for imaging systems (see figure 2.17). That means simply that, a given microscope may yield excellent image quality for a particular object, whereas it may be unsuitable for others. A fair comparison of imaging systems not only requires a full characterization of optical system and illumination, but also a consideration of the nature of the objects employed.

Chapter 3

The 46.9 nm Imaging System

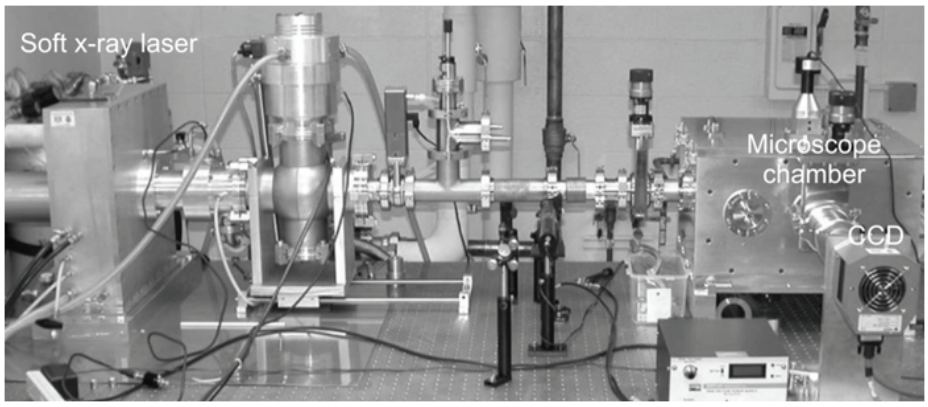

Figure 3.1: The EUV microscope operating at 46.9 nm illumination wavelength

Full-field microscopy with EUV lasers has been demonstrated first by our group using a compact microscope [36, 101], operating at a wavelength of 46.9 nm [140].

The microscope is illustrated in figure 3. Two spherical Sc/Si multilayer mirrors arranged in a Schwarzschild configuration with 16% throughput condense the light from the output of the laser onto the sample [34]. A zone plate lens with diameter 0.5 mm and numerical aperture (NA) 0.32 is used as the imaging objective lens [141]. This zone plate was produced by electron-beam lithography on 100 nm silicon nitride membranes. The zone plate was made free-standing, containing pseudorandomly located supportive spokes between the zones, to allow a throughput

near full 10% efficiency of the first diffraction order. This zone plate lens projects the image onto a charge-coupled device (CCD) detector with 13.5 μm pixels. The laser beam is created via a highly ionized plasma column that is generated by fast electrical discharge excitation of an Ar-filled capillary. It emits laser pulses higher than 10 μJ of energy ($¿\ 2.4 \cdot 10^{12} photons/pulse) and high monochromaticity (\Delta\lambda/\lambda = 5 \cdot 10^{-5}$) [140].

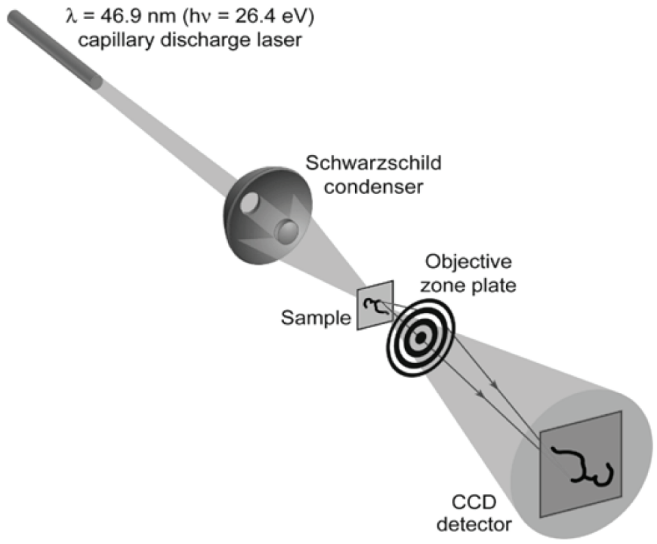

Figure 3.2: Schematic of the compact 46.9 nm microscope in transmission mode [36].

This microscope has demonstrated to be capable of obtaining near-wavelength spatial resolution with a single laser shot, corresponding to ∼1 ns temporal resolution, opening the possibility of investigating nanostructural dynamics. The entire microscope is extremely compact and occupies an area of 0.4 m×2.5 m.

Each of the optical elements are described in further detail in the subsequent sections.

3.1 Microscope illumination:

Ne-like Ar discharge-capillary laser

The laser output is created via a highly ionized plasma column generated in a capillary containing Ar. The excitation process in this collisionally pumped laser makes use of an ionization bottleneck technique to guarantee a high density of ions in a particular ionization state (see figure 3.3). The excited state can be produced mostly through collisions with plasma electrons from the ground state, although higher Ne-like excited states contribute by cascading from higher excited states. For the Ne-like ions, the population inversion is produced between the $1s^2 2s^2 2p^5 3p$ and $1s^2 2s^2 2p^5 3s$. Particularly, population inversion in the Ne-like Ar^{+8} ions results as the $2p^5 3p$ to $2p^6$ transition is dipole forbidden, while the $2p^5 3s$ to $2p^6$ is allowed with a high oscillation strength and a short lifetime, of the order of 1/3 ps.

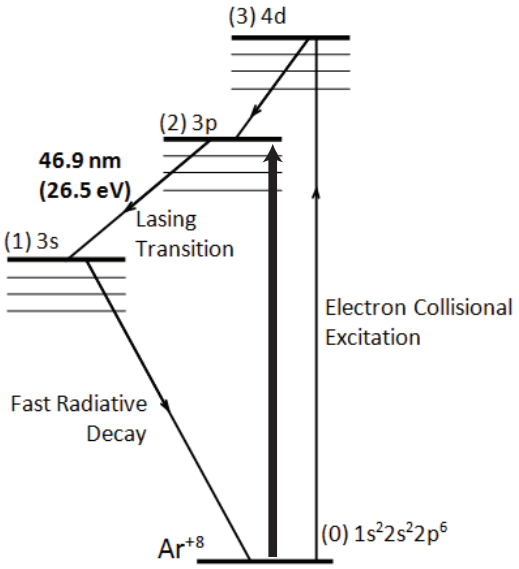

Figure 3.3: **Simplified energy level diagram for** Ar^{+8}. Ne-like ions are created in a hot dense plasma by direct collisional electron excitation to the 4d level from the ground state. The ions rapidly decay to the 3d and then to the 3p level. This transition is favored because the 4d to ground transition is diple forbidden. The decay to the 3s level leads lasing at 46.9 nm to occur. The 3s level has a relatively low population since it has a fast radiative decay to ground, about 1/3 ps. Therefore, the population inversion is built up between the 3p and 3s levels.

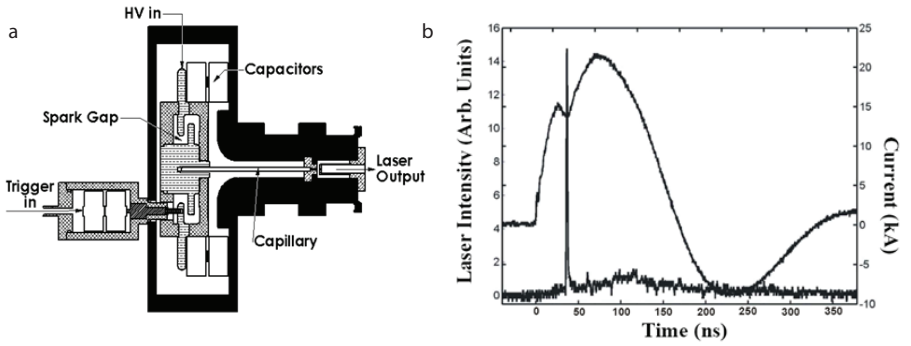

Figure 3.4: **a,** Schematic representation of the 46.9 nm discharge laser. **b,** Discharge current pulse and laser output pulse.

One of the critical aspects in capillary discharge lasers is the plasma column uniformity. The major cause of severe distortions of the plasma column is connected with axis inhomogeneities. High axial plasma uniformity is achieved through a pre-ionization of the Ar and subsequent fast discharge excitation of the capillary channel. The pre-ionized Ar gas that fills the capillary is compressed to form a dense and hot plasma column excited by a current pulse of 22 kA peak amplitude. The compression of the plasma column is induced by the magnetic field $\overrightarrow{B}$ that generates a radial force $\overrightarrow{F} = \overrightarrow{J} \times \overrightarrow{B}$, where $\overrightarrow{J}$ is the current flux across the capillary, giving a length to diameter ratio of the order of 1000:1 [142].

The firing of the laser begins with two delayed signals from a pulse generator, a 30 ms duration pulse and an impulse of 1 μs duration 29.7 ms after the first pulse starts. A *trigger box*, acting as a relay, remains open until it receives the first signal from the pulse generator. During these 30 ms, the relay enables a *high voltage power supply* to apply a 60 kV output voltage. During the 30 ms and 60 kV pulse, a parallel/series configuration capacitor set is charged while a pre-ionization current flows toward the capillary load. This pulse pre-ionizes the Ar gas upholding the necessary initial uniform plasma conditions for a stable compression. A *Thyratron* inside the *trigger box* makes use of the second signal created by the pulse generator by driving the short impulse to trigger a first pre-ionization spark gap from the parallel/series configuration set of capacitors.

The output voltage of the single-stage pulsed power unit is estimated to be of 80-90 kV. The pre-ionization spark gap creates a small current pre-pulse that increases the ionization level of Ar, charges a ring configuration ceramic capacitor set surrounding the second spark gap and connected to the laser head with a coaxial cable, igniting the discharge in the capillary, as shown in figure 3.4. The main spark gap is self-triggered to generate the 22 kA current pulse necessary to excite the plasma column and achieve conditions for amplification at 26.5 eV. Even though the collisional excitation scheme is typical of CW lasers, the inability to maintain the pump-power constant at the required levels limits the emission to pulsed laser generation with repetition rates up to 12 Hz.

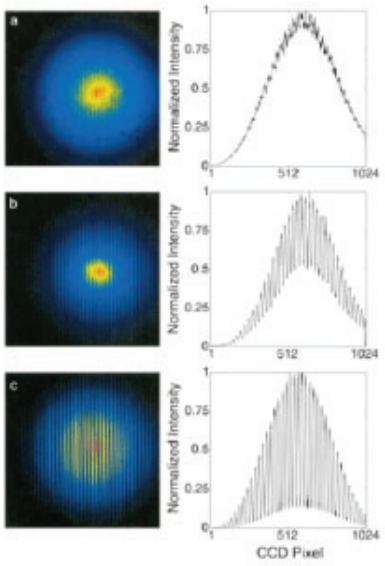

Figure 3.5: **a-c**, Representative interferograms and their lineouts showing the coherence buildup of the laser beam with increasing capillary length (a) 18 cm, (b) 27 cm and (c) 36 cm [143].

Under this pump mechanism, amplified spontaneous emission results in pulses of 1.5 ns duration at a wavelength of 46.9 nm (26.5 eV), with a spectral bandwidth of $\Delta\lambda/\lambda = 3.5 \cdot 10^{-5}$. The plasma in the capillary has a convex axis-symmetric electron density profile with an on-axis maximum that causes refraction of the amplified light. This provides a mode selection mechanism that filters higher-order modes and reduces the effective transverse source size significantly as the

gain medium lengthens. Therefore, the degree of coherence can be tailored by varying the plasma column length (see figure 3.5). The capillary length of 22 cm selected for the imaging experiments produces optimized, partially coherent pulses for illumination that limit speckle effects, as discussed previously, while providing $10\mu J$ pulse energies, equivalent to 2.4×10^{12} photons/pulse, sufficient photon flux for single-shot imaging.

3.2 The Imaging System

The output from the capillary discharge laser is collected by a multilayer condenser and focused onto the test sample. The condensed light travels through an absorption-sample and the objective zone plate forms an image onto the CCD.

3.2.1 The Condenser

The system utilizes a Schwarzschild configuration Sc/Si multilayer mirror [144] condenser [34] in order to focus the light on the sample. As discussed in chapter 2, at this wavelength the best monolayer mirrors exhibit a reflectivity no better than 10^{-4} at normal incidence, hence, multilayer coatings are required in order to pursue enhanced throughput. The condenser depicted in figure 3.6 consists of two concentric spherical mirrors. The primary convex mirror, 10.8 mm in diameter, and the secondary concave mirror, 50 mm in diameter, are coated with 60 Sc/Si

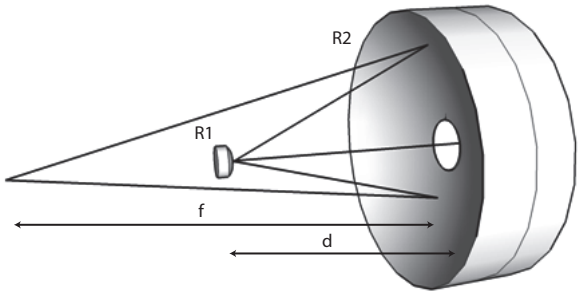

Figure 3.6: Layout of the Schwarzschild configuration Sc/Si multilayer mirror condenser.

layer pairs with a total reflectivity of nearly 40 % each at normal incidence. This particular design yields a condenser with NA = 0.18 and demagnification of ∼90 at a focal distance of 27 mm. In a Schwarzschild configuration, upon an adequate choice of R_1, R_2 and d, the aberrations of both mirrors are cancelled out for selected magnifications. Residual design aberrations become only apparent above the 5th order [145].

3.2.2 The Objective Lens

Free-standing zone plates are used as the imaging lenses. The microscope has been operated using four different zone plates, all with 500 μm diameter, and NAs 0.11, 0.19, 0.32, and 0.47, corresponding to 200, 120, 72.5, and 50 nm outer zone widths, and 2.13, 1.28, 0.77, and 0.48 mm focal lengths, respectively (see table 3.1).

Table 3.1:
Free-standing Objective Zone Plate Lenses: list of available objective lenses for the 46.9 nm imaging system displaying their numerical aperture (NA), outer zone-width (Δr), diameter (ϕ), focal length (f), depth-of-field (DOF), and expected resolution δ for incoherent (^{i}) and coherent (^{c}) cases.

NA	Δr [nm]	ϕ [mm]	f [μm]	**DOF** [μm]	$\delta^i - \delta^c$ [nm]
0.11	200	0.5	2132	3.41	120-250
0.19	120	0.5	1279	1.23	75-150
0.32	72.5	0.5	773	0.45	50-100
0.47	50	0.5	480	0.21	30-60

The zone plates were specifically designed to reduce absorption by making the ring structures free-standing, so their efficiency is maximized to be 10 % in first order. The zone plates were fabricated by electron-beam nano-lithography on 100 nm silicon nitride (Si_3N_4) membranes at the Center for X-ray Optics (CXRO) [141]. In order to fabricate the zone plates free-standing, the design incorporated a series of pseudo-randomly located spokes that connect all the consecutive zones and support the membrane beneath the zone plate in a free-standing structure.

3.2.3 The Detector

The formed image is capture by a 2048 x 2048 array CCD detector (model DO436 Andor Tech.). The system boasts negligible dark current with thermoelectric cooling down to - 30 C. The following table summarizes the main properties of the CCD:

Active Pixels	2048 x 2048
Pixel Size (W x H; μm)	13.5 x 13.5
Image Area (mm^2)	27.6 x 27.6
Max full frames per sec (1 MHz digitization)	0.2
Read Noise (e-, typical)	7.5 (1 MHz)
Count/photon at 26.5 eV	0.851

3.3 Resolution Characterization

The grating test was performed in order to assess the resolution of the 46.9 nm microscope. This work was carried out by Brewer et al., further described in reference [36]. The modulation response for three different zone plate objectives with numerical apertures 0.32, 0.19 and 0.12, which correspond to 73, 124, and 200 nm outermost zone widhts, respectively, was obtained by measuring the intensity modulation from single-shot images of gratings with different periods, as shown in figure 3.3. The spatial resolution was determined according to the Rayleigh-like cutoff, that is, the value of the grating half-period that exhibits an intensity modulation of 26.5 %.

3.4 Applications in Imaging

The 46.9 nm imaging system has demonstrated acquisitions with 50 nm spatial resolution using a single laser shot. The implementation of practical microscopes in the SXR region capable of rendering full-field images with wavelength-resolution and single ultrafast laser pulses is key to a vast number of applications, for ex-

ample, to structural biology studies. As reviewed in chapter 2, SXRs exhibit the potential to offer nanoscale spatial resolution with strong natural absorption and phase contrast. It was also reviewed that the interaction of SXRs with matter causes a high degree of ionization [146, 147], leading to possible structural changes and irreversible damage to the radiated sample. The radiation damage concerns

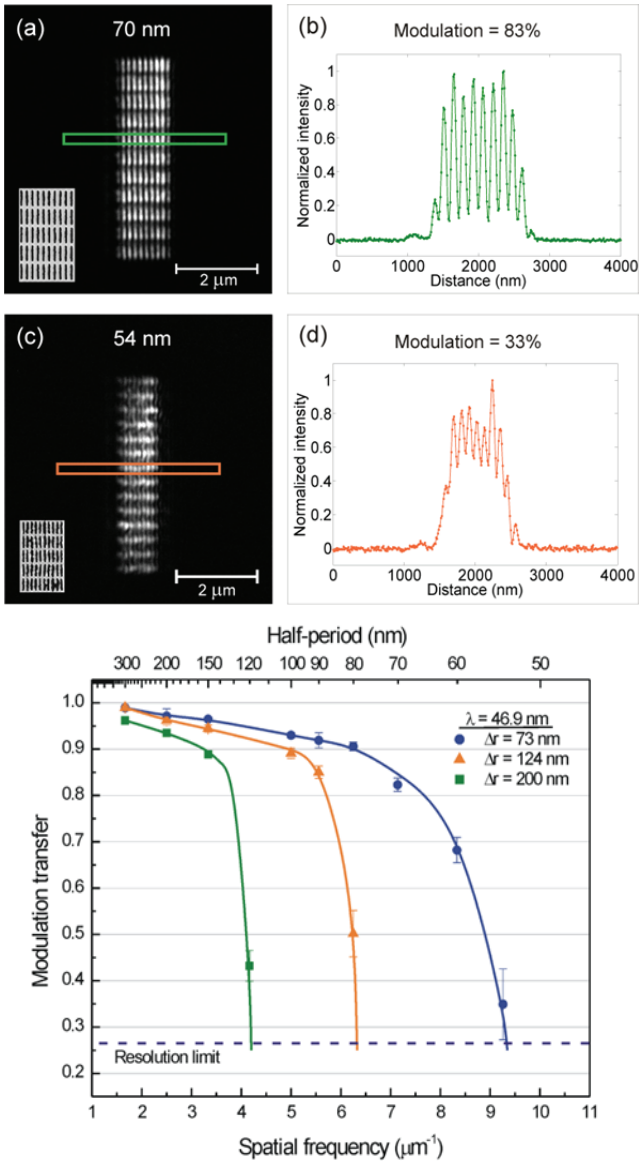

Figure 3.7: Single-shot images acquired with the 0.32 NA zone plate objective of **a,** a 70 nm half-period grating (with corresponding SEM image) and **b,** its corresponding lineout with an 83% intensity modulation; and **c,** a 54 nm half-period grating (with corresponding SEM image) with **d,** an intensity lineout showing an average modulation of 33%.**e,** Reconstructed modulation response with achieved half-period resolutions of 120, 80, and 54 nm for the 0.12, 0.19, and 0.32 NA objectives, respectively [36].

simply to the question whether the image recorded resembles the true biological structure or the results change with radiation doses. The radiation challenge becomes specially critical for living specimens. While the lethal radiation dose for most living organisms is about 1 to 10 Gy, typical doses for high resolution SXR imaging are of the order of 10^6 Gy, far beyond the damage threshold. The ability to rapidly flash a biological specimen with a single intense laser shot and acquire a bright-field image before the specimen is damaged or turned into a plasma would undoubtedly overcome any radiation-related alterations.

Towards this goal, the 46.9 nm imaging system has thus far assessed the feasibility to capture an image of dehydrated pancreatic tissue with a few laser shots, illustrated in figure 3.4. The sample consisted of a 45 nm thick mouse pancreas tissue cut fixed with glyceraldehydes after stained with osmium tetroxide and uranyl acetate and embedded in a glycerol-based aliphatic epoxy resin. From the image, different regions of the tissue were identified, such as islets of Langerhans, which are clusters of several types of cells active in producing hormones, or acinar cells, responsible for secreting digestive enzymes.

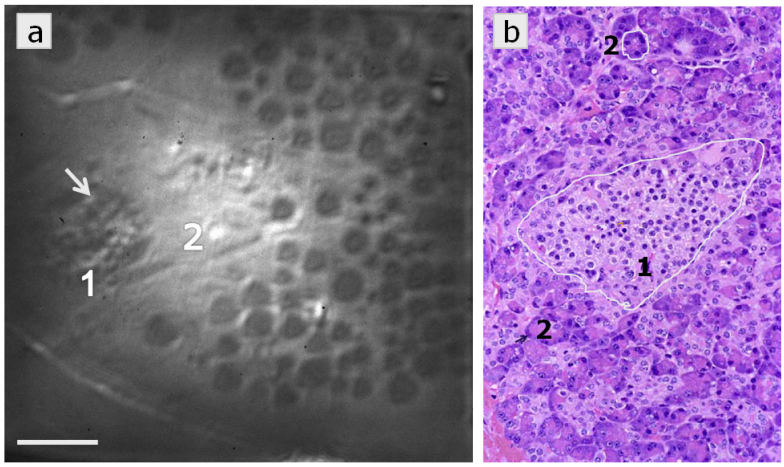

Figure 3.8: Pancreatic tissue. **a, SXR image** of pancreatic tissue. Exposure time 20 seconds at 2 Hz repetition rate. Islets of Langerhans **(1)**, pancreatic acini **(2)**, and the acinar nucleus **(arrow)** are identified (bar = 2 μm). **b, Light Microscope Photomicrograph** of 5 μm thick section of hematoxylin and eosin stained mouse pancreas.

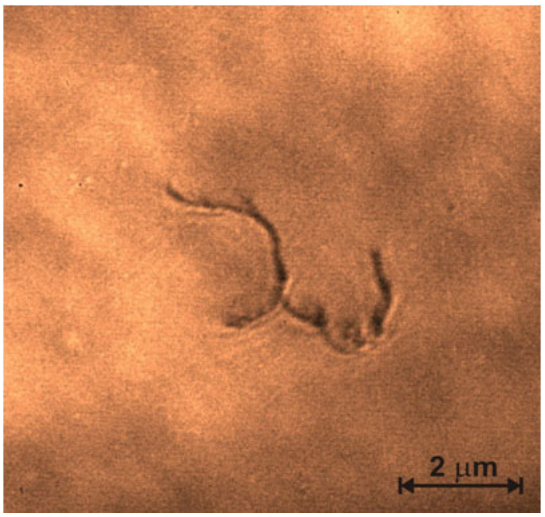

Figure 3.9: Single-shot bright-field acquisition of a C-nanotube entanglement (nominal diamater 50 nm) using the 46.9 nm imaging system with an objective lens of 0.32 NA [36].

The success in demonstrating single-shot SXR imaging of living specimens will also rely on the fabrication of highly efficient membranes and cavities that serve as specimen holders. These holders enable biological specimens to survive vacuum environments enclosed in sealed cavities and are constructed such that their efficiency in the SXR region is maximized. Much work has been dedicated to the development of these holders, further described in the appendix.

Another application to the capability to acquire high-resolution single-shot images is the recording of nanoscale ultrafast dynamics. The image shown in figure 3.4 was acquired with a single shot by Brewer et al. and displays an entanglement of carbon nanotubes with nominal diameter of 50 nm. An extension of this demonstration is the acquisition of multiple sequenced snapshots of nanoscale events evolving in time, and hence, the recording of nanoscale movies. This idea is elaborated and demonstrated in the following chapter.

Chapter 4

Sequential single-shot SXR Microscopy

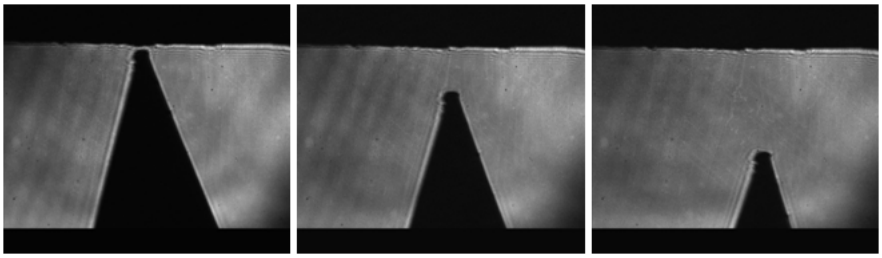

Figure 4.1: SXR snapshots of an atomic force microscope tip in motion.

The development of high energy per pulse table-top soft X-ray lasers have set the ability to freeze any arbitrary motion by acquiring full-field images in a single laser shot in real-space. This chapter is dedicated to the first demonstration of dynamic flash imaging employing a compact SXR microscope by means of the 46.9 nm imaging system described in the previous chapter. Requiring little sample preparation and operable in transmission or reflection configuration, the microscope has proven the ability to effectively achieve near-wavelength spatial resolution [101] and capture images with a single laser shot [36] to record nanoscale dynamic interactions through sequential single-shot acquisitions.

4.1 Introduction to Dynamic Imaging

Filmmaking smaller and faster has unconditionally set the trend for researchers studying dynamic phenomena through time-resolved imaging, regardless of the technique. There is a wide variety of areas of interest that today remain relatively unexplored where dynamic processes at atomic-scales occur on very short to ultrashort timescales (10^{-6} to 10^{-15} seconds). This sections aims to briefly review the main advances in imaging systems towards this goal.

Imaging the dynamics of ultrafast processes is possible using stroboscopic pump and probe techniques. In these experiments, a pump pulse triggers a process and a probe pulse samples the state at which the system is a certain time after the stimulus has been applied. Through this approach, the temporal resolution is only limited by the pulse width. However, it is necessary that during the image acquisition time the state of the sample remains unaltered.

While the temporal resolution in conventional microscopes is limited to the detector readout rate, time-resolved visible microscopy has accomplished to reduce the gap through pump and probe experiments down to the femtosecond range, although achieved spatial resolutions have never reached beyond a few micrometers [148, 149].

Alternatively, transmission electron microscopy can reach sub-Å spatial resolution, although using the standard electron thermionic cathode cannot be used to image fast dynamics. Two different approaches have been implemented to image dynamics. In one of them, an ultrafast laser is used to generate an electron bunch with only a few electrons per pulse and the same laser is used to trigger the dynamic process on the sample at a delayed time. The image is formed in a scanning geometry from the scattering of thousands of single-electron bunches, so the spatial (sub-Å and temporal resolution (fs) are maximized [61, 62]. However, this imaging scheme requires the dynamic subject of study to be strictly repetitive [150]. In

Figure 4.2: Example of a single-shot SXR image: an atomic force microscope tip.

the other approach, Armstrong et al. have successfully demonstrated single-shot acquisitions in transmission electron microscopy with exposures as short as a few tens of nanoseconds [63, 151]. This technique also relies on laser excitation of the cathode to generate short (10 ns) electron pulses with ¿ 10^7 e-/pulse), ultimately limiting the spatial resolution to ∼60 nm [64] due to stochastic blurring and space charge effects. These technological constraints do not apply to SXR imaging. Furthermore, imaging in the SXR region overcomes the low electron penetrating power, provides element specificity, and allows more flexible imaging conditions, e.g., the presence of electromagnetic fields.

Various X-ray imaging techniques such as zone plate based full-field and scanning microscopy, holography and coherent diffractive imaging are currently being developed to offer enhanced temporal and spatial resolutions [152, 37, 78, 46, 80, 75, 153]. However, most of these techniques exhibit the same limitation as that of the approach developed by Zewail et al., i.e., full repeatability in order to build an image. Specific to freezing the rapid motion of non-repetitive mechanisms, it is essential not only to feature very short pulse durations but also that these pulses contain sufficient amount of photons to enable single-shot acquisitions. The access to soft X-ray imaging systems capable of taking images in a single shot to study transient behaviors is, nonetheless, extremely reduced and primarily limited to a handful of compact laser and free electron lasers (FEL) sys-

tems [36, 43, 154, 58, 59]. FELs have indisputably revealed a revolutionary merge of light attributes by owning the possibility to record the coherent diffraction pattern from the sample before it is destroyed by a single ultrashort intense laser pulse. As of today, there has only been one demonstration of sequenced single-shot soft X-ray imaging of ultrafast nanoscale dynamics, reported in reciprocal space and achieving sub-100 nanometer spatial resolution at FLASH in Hamburg [39].

This chapter describes the results on the first full compilation of sequential single-shot images depicting nanoscale dynamic interactions using a compact SXR microscope. The images were acquired non-invasively and employing imaging optics, hence necessitating no further image processing.

4.2 Experimental Setup

The experiment consisted of imaging the motion of an oscillating magnetic nanoprobe perturbed by stray magnetic fields from an array of magnetic strips, resembling the configuration of magnetic force microscopes (MFMs) [155]. These results could substantially reach out to applications where a direct visualization was previously unattainable yet highly desired. For example, nanocantilevers are increasingly attracting attention because of their potential to become a new generation of ultrasmall sensors for biotechnology and data storage [156, 157], among others. The ability to monitor the motion of these nanocantilevers subject to their surrounding force fields would introduce a unique approach to the characterization of their mechanical properties, complementary to other efforts subject of innumerable studies. Furthermore, based on previous demonstrations, this technique is now wavelength scalable and accessible to spatial and temporal resolutions of a few tens of nanometers and a single picosecond, respectively [158, 114, 159]. We envision these tools will soon unfold the unseen in emerging nanotechnologies.

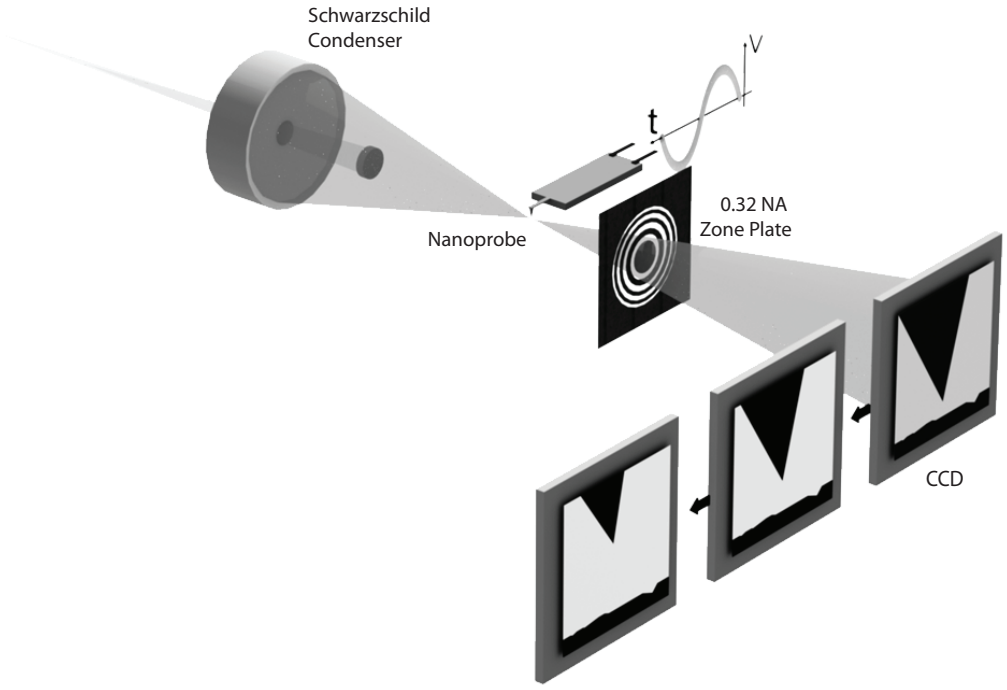

Figure 4.3: Sequential single-shot imaging of dynamic interactions.

The general layout of the experiment is depicted in figure 4.3. The Schwarzschild condenser focuses a single incident pulse from soft X-ray laser into a nanoprobe tip on an oscillating cantilever. The cantilever is mounted onto a piezoelectric bimorph that is set to vibrate at a frequency equal to the cantilever's natural resonance frequency for in order to mechanically couple its actuation. At a given instant, a bright-field image of this tip in motion is directly formed on a CCD detector through by a 0.32 NA free-standing zone plate objective lens. A series of time-delayed real-space images illustrating the evolution of the tip dynamics is captured by synchronizing the soft X-ray laser trigger and the device drive signal.

Two different nanoprobes were employed for various demonstration purposes. A high-aspect ratio standard atomic force microscope (AFM) was used to demonstrate sequential single-shot imaging of a nanoscopic object. The time-delay step for the sequence of snap shots was chosen to be nominally 30 ns, so that a total of about 100 images reconstruct the rapid periodic motion with frequency $f = 318.6$ kHz ($T = 3.14\mu s$) and amplitude ± 250 nm.

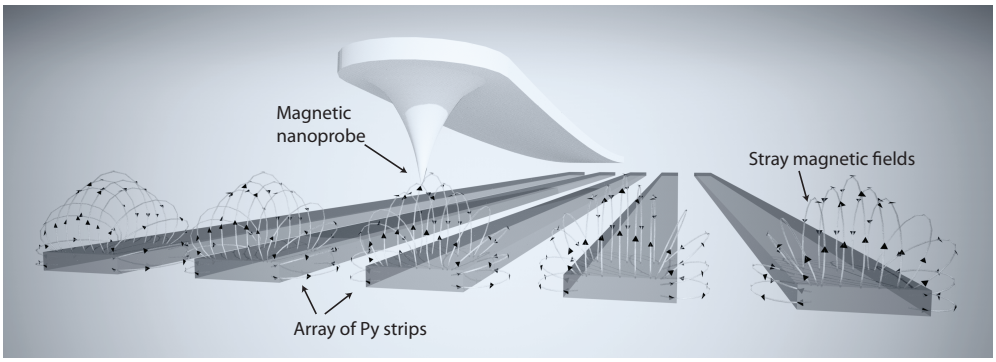

Figure 4.4: Representation of the interaction between an oscillating magnetic nanoprobe and the stray fields from an array of magnetic strips.

The second part of the experiment employed a Co-alloy coated magnetic force microscope (MFM) tip to demonstrate the capability of single-shot flash imaging and reveal perturbations on the motion of the nanoprobe due to interactions with surrounding magnetic force fields. The interaction scenario is depicted in figure 4.4, where the nanoprobe is made to oscillate with an amplitude of ± 500 nm above an array of Permalloy strips at a minimum separation distance of 150 nm. These strips exhibit strong uniaxial shape anisotropy and hence remain magnetized along the x axis at remanence. The stray magnetic field is the largest at the end of the microstrip (see figure 4.5). As will be shown, the nanoprobe experienced a strong interaction above any strip and none in between strips.

4.3 Methods

4.3.1 Samples

Nanoprobes

The experiment was conducted utilizing two different commercially available nanoprobes. The first, a 5:1 high aspect ratio atomic force microscope (AFM) probe, featured a 20 nm radius Si tip on a 125 μm long cantilever, spring constant

of 40 N/m, and resonance frequency of 318.6 kHz. The second, a Co-alloy coated magnetic force microscope (MFM) probe, had a resonance frequency of 65 kHz, a nominal spring constant of 0.7 N/m, and a coated tip-radius of 40 nm fabricated at the end of a 230 μm long cantilever. The Co-alloy coating allows steady permanent magnetization in the direction of the tip axis. The tip was pre-magnetized prior to running the experiment by a strong Nd magnet. Both tips were clamped onto a rectangular bimorph actuator driven by an AC signal at a frequency corresponding to their resonant frequencies. The voltage was adjusted to select a desired amplitude of cantilever oscillation.

Magnetic sample

A 1:1 array of Permalloy strips with dimensions $10\mu m \times 2\mu m \times 40nm$ were fabricated on a Si substrate by means of UV photo-lithography, magnetron sputtering, and a lift-off process. A Si substrate was first cleaned, pre-baked for 60 seconds at 90 °C, spin-coated with 300 nm of positive photo-resist Shippley 1818 and post-baked at 120 °C for 90 seconds. The photo-resist was then exposed to a 15 mW UV lamp for 10 seconds through two absorptive masks simultaneously (the $1^{st} with 1:12\mu m$ spaces and lines, the $2^{nd} with 10\mu m \times 10\mu m$ clear squares) located on the edges of the Si substrate. The exposed photo-resist was developed with

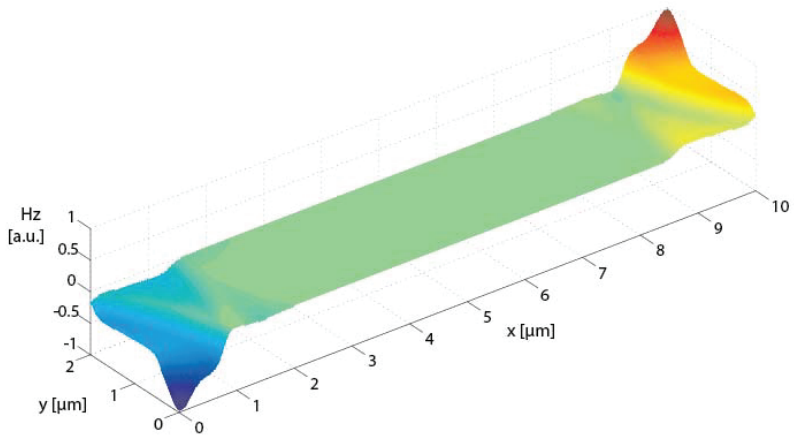

Figure 4.5: Normalized remanent magnetic field strength z-component at z = 150 nm from the surface of a single Permalloy strip after saturation along the x axis.

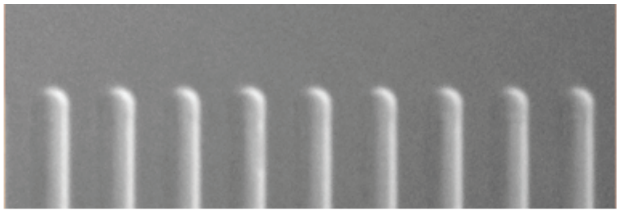

Figure 4.6: Dark-field image of the fabricated array of 1:1 $10\mu m \times 2\mu m \times 40nm$ Permalloy strips.

a 4:1 solution of distilled water and AZ 400K developer for 60 seconds, resulting in cleared 1:1 arrays of the design dimensions. In order to clean the surface of the target, pre-sputtering was carried out for 120 seconds before the film growth. A 40 nm thin film of Permalloy with composition of Ni/Fe 81:19 wt% was then deposited on the patterned array through DC magnetron sputtering . The base vacuum before sputtering was 7.410^{-8} $Torr$ and the target-substrate distance was 30 cm. The DC power was 15 W (342 V and 43 mA). During the sputtering, 3.3 $mTorr$ of Ar filled the growth chamber, resulting in a growth rate of 0.97 nm/min. The fabrication of Permalloy strips was finalized through lift-off, rinsing the sample in an acetone bath for 60 minutes (see figure 4.6).

4.3.2 Magnetic Force Interaction Model

A magnetic cantilever interacting with stray magnetic fields can be modelled as a frequency-locked harmonic oscillator. This interaction results in changes in due to a frequency shift in the natural resonance curve of the harmonic oscillator which is proportional to the presence of force gradients. This is called the *perturbed harmonic oscillator* model. Let us begin with the fundamentals of the perturbation.

Within this model, the presence of a magnetic force gradient from the Permalloy strip acts to modify the effective spring constant of the cantilever and change its resonant frequency. Let us represent the tip with its spring constant k_0. The derivative of of the exerted force $F(x, y, z)$ as a function of the distance between

the tip and the strip, z, can be represented in the form of a spring constant $k_f = -\partial F/\partial z$. With this simple representation, the cantilever can be modelled with an effective spring constant modified by a z-dependent term corresponding to the force gradient as

$$k_{eff} = k_0 + k_f = k_0 - \frac{\partial F}{\partial z} \tag{4.1}$$

A direct consequence of a varying spring constant is a varying resonance frequency ω_r. For a harmonic oscillator with effective mass m

$$\omega_r^2 = \frac{k_{eff}}{m} = \frac{1}{m}\left(k - \frac{\partial F}{\partial z}\right) \tag{4.2}$$

Notice that the resonant frequency of the system is now a function of z, hence, it will change depending on the position of the tip with respect to the surface of the strip. The variable term of the resonance frequency, the *frequency shift* $\Delta\omega(z)$, is related to the unperturbed natural frequency of the cantilever ω_0 as $\omega_r^2(\mathbf{z}) = [\omega_0 + \Delta\omega(\mathbf{z})]^2$. From equation 4.2, under the approximation that $\Delta\omega \ll \omega_0$,

$$\frac{\Delta\omega}{\omega_0} = -\frac{1}{2k}\frac{\partial F}{\partial z} \tag{4.3}$$

Typical values of $\partial F/\partial z$ lie below 10^{-2} N/m, which, in the range of 100's of KHz, results in a frequency shift $\Delta\omega$ of only a few Herz at most. The amplitude in a frequency-locked harmonic oscillator varies as a consequence of these few hertz of resonance frequency shift. The resonance line-shape $A(\omega)$ of a cantilever is characterized by a Lorentzian of the form

$$A(\omega) = \frac{A_0(\omega_0/\omega)}{\sqrt{1 + Q^2\left(\omega/\omega_0 - \omega_0/\omega\right)^2}}, \tag{4.4}$$

where $Q = \omega_0/\Delta\omega$ is the quality factor of the cantilever. As equation 4.4 shows,

a change in amplitude is maximized for small $\Delta\omega$ when ω lies in the maximum slope at $A(\omega = \omega_{max})$, which occurs at $\omega_0/\sqrt{8}Q$ from the maximum on either side of the curve. That is,

$$\omega_{max} = \omega_0 \left(1 \pm \frac{1}{\sqrt{8}Q}\right), \tag{4.5}$$

and at this point of the curve, its derivative

$$\left[\frac{\partial A}{\partial \omega}\right]_{\omega=\omega_{max}} \simeq \frac{4A_0Q}{3\sqrt{3}\omega_0} \tag{4.6}$$

Recalling equation 4.3 and plugging it into the equation 4.6, the change in amplitude produced by a force gradient when the oscillator is being driven at a frequency ω_{max} is given by

$$\Delta A \simeq \left(\frac{2A_0Q}{3\sqrt{3}k}\right)\frac{\partial F}{\partial z} \tag{4.7}$$

We are almost ready to predict the amplitude shift, since most parameters in the equation above are given:

A_0	800 nm	given by the experiment
Q	1E2	nominal (manufacturer)
k	0.7 N/m	nominal (manufacturer)

Let us estimate the magnetic force as the interaction force between two point magnetic dipoles with magnetic moments $\mathbf{m}_{Py}$ and $\mathbf{m}_{tip}$ corresponding to the strip and the magnetic probe, respectively. A single $10\mu m \times 2\mu m \times 40nm$ Permalloy strip ($M_{Py} = 800emu/cm^3$) exhibits a magnetic moment magnitude in x of $\mathbf{m}_{Py} = 6.4 \times 10^{-13} Am^2$, while a 40 nm cone shaped Co-alloy ($M_{Co} = 1400emu/cm^3$) coated tip has an approximate magnetic moment magnitude in z of $\mathbf{m}_{tip} = 4.1 \times 10^{-17} Am^2$ [160].

The magnetic field created by a single dipole is expressed as

$$\overrightarrow{B}(r) = \frac{\mu_0}{4\pi}\frac{1}{r^3}\left[3(\overrightarrow{m}_{dip}\cdot\widehat{r})\widehat{r} - \overrightarrow{m}\right] \tag{4.8}$$

We extract the component of the magnetic field only in z and express it in Cartesian coordinates as

$$\overrightarrow{B}_Z(z) = \frac{\mu_0}{4\pi}\frac{3}{z^3}|\overrightarrow{m}_{dip}|\cos\phi\cos\theta\sin^4\theta(\widehat{z}) \tag{4.9}$$

and its derivative

$$\frac{\partial\overrightarrow{B}_Z}{\partial z}(z) = -\frac{\mu_0}{4\pi}\frac{9}{z^4}|\overrightarrow{m}_{dip}|\cos\phi\cos\theta\sin^4\theta(\widehat{z}) \tag{4.10}$$

Therefore, a magnetic dipole with magnetic moment $\mathbf{m}_2$ experiences a force in terms of the energy gradient such that for the z component

$$F_Z(z) = \nabla(\mathbf{m}_2|\overrightarrow{B}_Z|) = \mathbf{m}_2\frac{\partial\overrightarrow{B}_Z}{\partial z} \tag{4.11}$$

By substituting $\mathbf{m}_2 = \mathbf{m}_{tip}$, $\mathbf{m}_{dip} = \mathbf{m}_{Py}$, and recalling equation 4.7, we estimate the the amplitude shift to be

$$\Delta A = |\overrightarrow{m}_{tip}|\frac{2A_0Q}{3\sqrt{3}k}\frac{\partial^2\overrightarrow{B}_Z}{\partial z^2} \tag{4.12}$$

which is expected to be of a only a few tens of nanometers at its maximum, as shown in figure 4.3.2.

The contribution of a complete array of Permalloy strips to the amplitude shift would be periodic with line-space distance period, hence, it can be readily represented as a function of z. Figure 4.3.2 exemplifies the case when $z = 150nm$, the

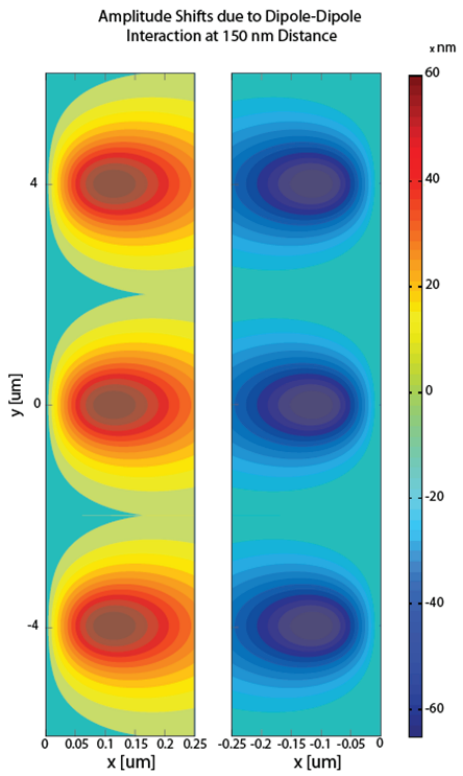

Figure 4.7: Estimated amplitude shift as a result of the interaction between the Permalloy strip and the Co-alloy coated oscillating tip at a separation distance of z = 150 nm for the two possible magnetizations of the strip across x.

lowermost unperturbed position of the tip in the experiment.

4.4 Experimental Results

4.4.1 Natural Harmonic Oscillation

A series of sequential non-destructive images was acquired and assembled into a movie that depicts the complete motion of the tip oscillating at $f = 318.6$ kHz with an amplitude of ± 250 nm and placed a few hundreds of nanometers off a reference surface. The instant at which the image was taken with respect to the phase of the oscillation was determined from the laser-generated current pulse and was monitored at all times to guarantee the synchronization of the acquisitions. Figure 4.4.1 a-d show a sequence of flash images of the tip at different times in the oscillation. The trajectory of the tip was reconstructed (figure 4.4.1 e) from

$\sim$ 100 images acquired over several cycles of oscillation.

An ensemble of images was formed with all the acquired flash images at different times under the same oscillatory and illumination conditions. The location of the tip in the images was analyzed by first equalizing the background of all the full-field (23×23 μm^2) images from each ensemble of images in order to compensate for shot-to-shot brightness variations. The tip location was then roughly

estimated through a gradient map of the background-equalized image. In order to retrieve the distance between the reference surface and the tip, the equalized image was cropped into a 250×250 pxl^2 sub-image centered at the estimated location of the tip and mapped into a 10× intensity-interpolated image. Each pixel in the image corresponds to 11.37 nm (M $\sim$ 1200). Finally, the surface-tip separation distance was obtained by a normalized 3-pixel averaged intensity cross-section. As a result, from the compilation 100 time-delayed images, the period motion of the tip was completely reconstructed within an error of approximately ±1 pixel, that is, ±11.37 nm.

4.4.2 Perturbed harmonic oscillator

Following the same image-acquisition and -analysis procedure, the perturbed oscillation of the magnetic nanoprobe was captured under three scenarios: (1) on top of a Py strip-edge, (2) in between two strips, and (3) on top of the neighboring Py strip-edge. Scenarios (1) and (3) were implemented for repeatability purposes. The nanoprobe was naturally oscillating with a ±500 nm amplitude and frequency 65.2 kHz at a minimum separation distance of 150 nm. As the resonating magnetic nanoprobe approached the edge of either Py strip, the present force gradients deflected the tip towards the substrate surface. According to the model, at 150 nm the frequency shift in the resonance curve of the cantilever would be of about $\Delta\omega \approx -10 rad/sec$, leading to a positive amplitude shift of a few tens of nanometers.

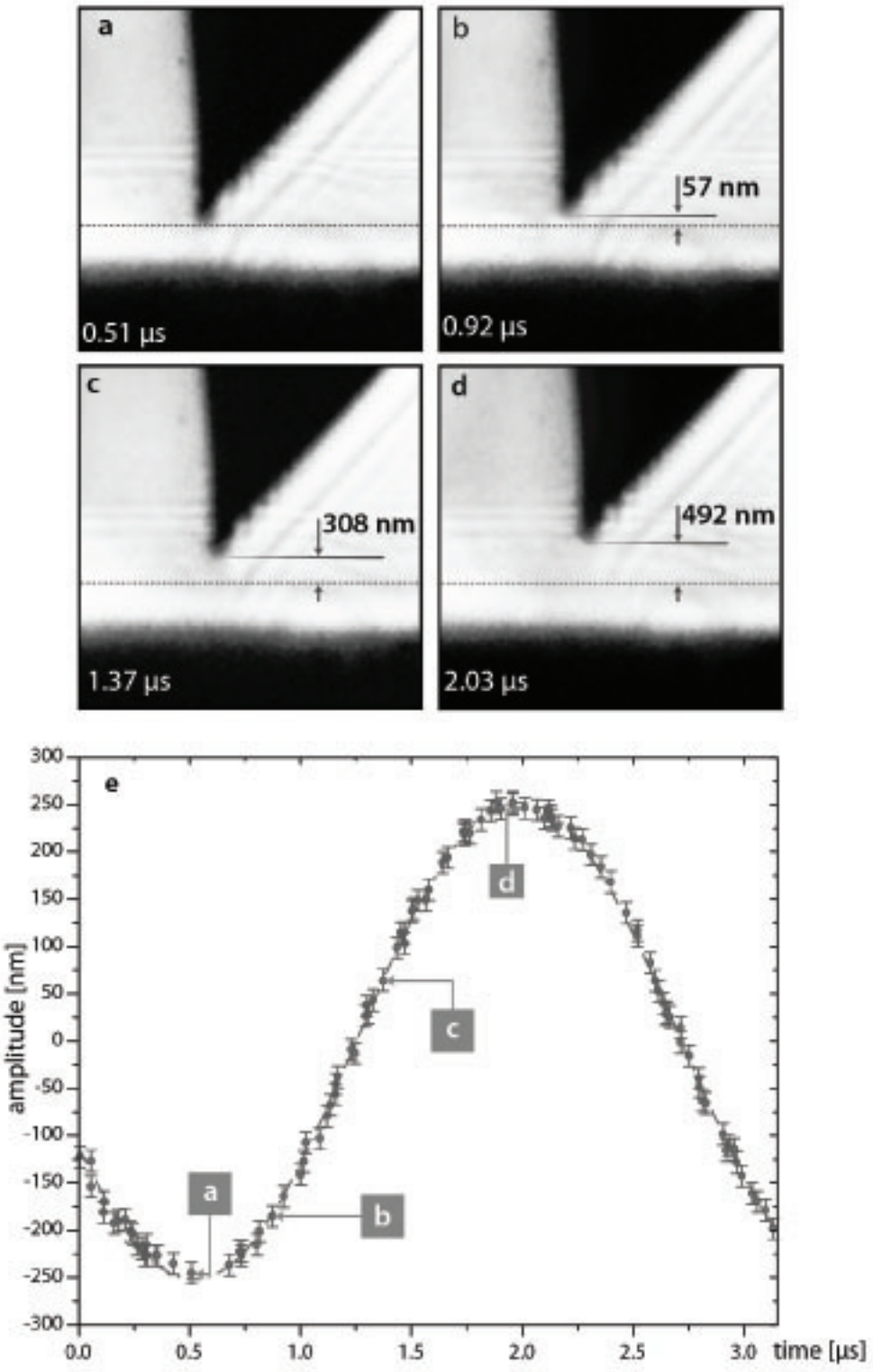

Figure 4.8: **a-d,** Time-delayed sequential SXR images illustrating the motion of a nanorpbe tip oscillating at a resonance frequency of 318.6 kHz with an oscillation amplitude of ±250 nm. **e,** A total of 100 single-shot images reproduce the motion of the tip over a full period.

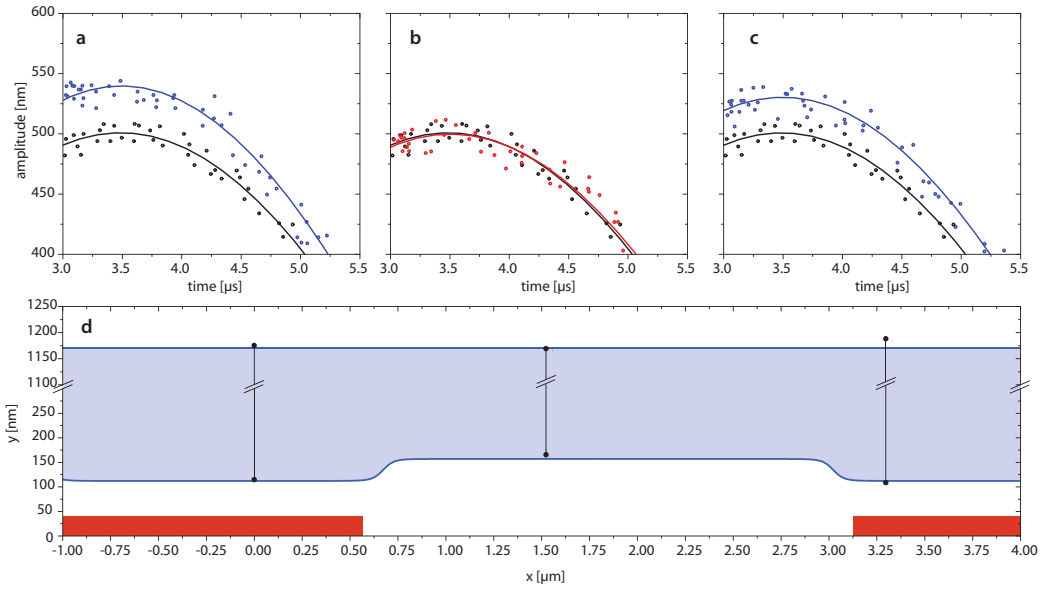

Figure 4.9: **a-c,** Relative reconstruction of the perturbed oscillations (above the strips) in blue **(a and c)** and no measurable perturbation (in between strips) in red **(b)** compared to the natural oscillation of the cantilever in black.**d,** Measured (black) and modelled (blue) extrema of the tip oscillation.

From the analysis of the single-shot time-delayed images, the tip trajectory was reconstructed for each of the interaction scenarios described above, shown in figures 4.4.2 **a-c**. In these figures, the natural oscillation far from the sample is shown in the black trace for comparison purposes. From the average of five independent oscillation fits, increases in the amplitude of the oscillation of 40 $\pm$ 3.29 nm and 30 $\pm$ 2.04 nm with respect to the tip natural oscillation amplitude were measured for **a** and **c** respectively. No amplitude change was measured when the oscillating tip was located in between the strips **b**. Figure 4.4.2 **d** illustrates the extrema of the tip oscillation (black dots) relative to the magnetic surface determined for the cases plotted in 4.4.2 **a-c**. The red rectangles represent the Permalloy strips. This figures integrates in blue shading the estimated amplitude of oscillation due to the interaction with the stray magnetic fields as a function of transverse position across the edge of the substrate predicted by the model in section 4.3.2. The estimated loci of the tip during a show very good agreement with the experimental results.

Chapter 5

Final Remarks and Outlook

Single-shot flash SXR imaging has been demonstrated for the first time using any compact SXR source by acquiring single-shot images directly using a free-standing zone plate. Therefore, a sequence of snapshots was readily acquired directly in real-space, that is, without requiring any post-processing, and non-destructively, thus, without altering the structural dynamics of the sample.

A direct recording of the motion of a magnetic force microscope tip in resemblance to its normal operation has been demonstrated. The perturbed oscillation of the magnetic nanoprobe due to magnetic force interactions has also been recorded and fully characterized. These results demonstrate the capability to acquire sequential single-shot images of nanoscale phenomena using bright flashes from a SXR laser, directly in real-space, with one nanosecond temporal resolution and nanometer-scale spatial resolution on a table-top.

The ability to readily visualize motions in the nanoscale can now be extended to a wide variety of research areas where a direct observation of rapid arbitrary motions in nanoscopic objects was unattainable. The technique opens new ways to study nanoscale processes in material science and nanotechnology because it allows for the rapid visualization of dynamic nanoscale phenomena in a very compact setup. This means that researchers developing new NEMS, for instance, will

be able to use it to readily visualize in their own lab the nanometer-scale motion of their nanodevices, potentially accelerating the development of that given technology.

Moreover, this microscope has been proven in the past to operate in reflection configuration [101]. A straightforward extension of this technique to sequential single-shot reflection imaging can allow the recording of material surface dynamics, such as nanomachining processes [103] or crystal twinning dynamics [161], are readily available now. This demonstration, implemented in a compact laboratory setting, constitutes a key step towards thoroughly contributing to the fundamental understanding of nanoscale dynamic processes.

Furthermore, this technique will soon be implemented in the ultrafast regime owing to recent advances in saturated table-top SXR lasers that are capable of providing high pulse energies in the ultrafast regime. More specifically, a saturated table-top SXR laser provides now one picosecond pulses with energies ¿ 10 μJ at a wavelength of 13.9 nm [158]. Therefore, single-shot SXR flash imaging is now extendable to visualize ultrafast dynamics on a table-top.

Bibliography

[1] R. Hooke, *Micrographia: or, Some physiological descriptions of minute bodies made by magnifying glasses*. London: J. Martyn and J. Allestry, 1665.

[2] E. Abbe, "Beiträge zur Theorie des Mikroskops und der mikroskopischen Wahrnehmung," *Archiv für Mikroskopische Anatomie*, vol. 9, pp. 413–418, Dec. 1873.

[3] E. Abbe, "Note on the proper definition of the amplifying power of a lens or a lens system," *J R Microsc Soc*, vol. 4, pp. 348–351, 1884.

[4] R. A. Zsigmondy, "Properties of colloids," *Nobel Lecture*, December 11, 1926.

[5] F. F. Zernike, "Phase-contrast, a new method for microscopic observation of transparent objects. Part I," *Physica*, vol. 9, pp. 686–698, 1942.

[6] F. F. Zernike, "Phase-contrast, a new method for microscopic observation of transparent objects. Part II," *Physica*, vol. 9, pp. 974–986, 1942.

[7] E. Ruska, "The Development of the Electron-Microscope and of Electron-Microscopy (Nobel Lecture)," *Angewandte Chemie-International Edition in English*, vol. 26, pp. 595–605, July 1987.

[8] M. Born, E. Wolf, and A. Bhatia, *Principles of optics: electromagnetic theory of propagation, interference and diffraction of light*. Cambridge University Press, 1999.

[9] E. G. van Putten, D. Akbulut, J. Bertolotti, W. L. Vos, A. Lagendijk, and A. P. Mosk, "Scattering lens resolves sub-100 nm structures with visible light," *Phys. Rev. Lett.*, vol. 106, p. 193905, May 2011.

[10] J. Pawley, *Handbook of biological confocal microscopy*. The language of science, Plenum Press, 1995.

[11] G. Normanski and A. R. Weill, "Application a la metallographie des methodes interferentielles a deux ondes polarisees," 1955.

[12] S. Paddock, *Confocal microscopy methods and protocols*. No. v. 122 in Methods in molecular biology, Humana Press, 1999.

[13] K. R. Porter and J. Blum, "A study in microtomy for electron microscopy," *The Anatomical Record*, vol. 117, pp. 685–709, 1953.

[14] J. Goldstein, *Scanning electron microscopy and x-ray microanalysis*. No. v. 1, Kluwer Academic/Plenum Publishers, 2003.

[15] K. Klein, I. Anderson, and N. de Jonge, "Transmission electron microscopy with a liquid flow cell," *Journal of Microscopy*, vol. 242, no. 2, pp. 117–123, 2011.

[16] de Jonge, "Electron microscopy of specimens in liquid," *Nature Nanotechnology*, vol. 6, pp. 695–704, 2011.

[17] C. O. Girit, J. C. Meyer, R. Erni, M. D. Rossell, C. Kisielowski, L. Yang, C.-H. Park, M. F. Crommie, M. L. Cohen, S. G. Louie, and A. Zettl, "Graphene at the edge: Stability and dynamics," *Science*, vol. 323, no. 5922, pp. 1705–1708, 2009.

[18] W. Roentgen, *Eine neue Art von Strahlen*. Verlag und Druck der Stahelschen K. Hof- und Universitts-Buch- und Kunsthandlung, 1896.

[19] A. Engstroem *Acta Radiol. Suppl.*, 1946.

[20] D. Attwood, *Soft x-rays and extreme ultraviolet radiation: principles and applications*. Cambridge University Press, 2000.

[21] R. Carlton, A. Adler, and E. Frank, *Principles of radiographic imaging: an art and a science*. No. v. 1, Thomson Delmar Learning, 2006.

[22] "http://www.xradia.com."

[23] P. C. D. et al., "Synchrotron x-ray tomographic microscopy of fossil embryos," vol. 442, pp. 680–683, 2006.

[24] S. C. Mayo, P. R. Miller, S. W. Wilkins, T. J. Davis, D. Gao, T. E. Gureyev, D. Paganin, D. J. Parry, A. Pogany, and A. W. Stevenson, "Quantitative x-ray projection microscopy: phase-contrast and multi-spectral imaging.," *Journal of Microscopy*, vol. 207, no. Pt 2, pp. 79–96, 2002.

[25] T. E. Gureyev and S. W. Wilkins, "On x-ray phase imaging with a point source," *J. Opt. Soc. Am. A*, vol. 15, pp. 579–585, Mar 1998.

[26] S. Mayo, T. Davis, T. Gureyev, P. Miller, D. Paganin, A. Pogany, A. Stevenson, and S. Wilkins, "X-ray phase-contrast microscopy and microtomography," *Opt. Express*, vol. 11, pp. 2289–2302, Sep 2003.

[27] E. M. F. et al., "Phase-contrast x-ray microtomography links cretaceous seeds with gnetales and bennettitales," vol. 450, pp. 549–553, 2007.

[28] C. M. Schneider, K. Meinel, J. Kirschner, M. Neuber, C. Wilde, M. Grunze, K. Holldack, Z. Celinski, and F. Baudelet, "Element specific imaging of magnetic domains in multicomponent thin film systems," *Journal of Magnetism and Magnetic Materials*, vol. 162, no. 1, pp. 7 – 20, 1996.

[29] J. B. Kortright, S.-K. Kim, H. Ohldag, G. Meigs, and A. Warwick, "Magnetization imaging using scanning transmission x-ray microscopy," *AIP Conference Proceedings*, vol. 507, no. 1, pp. 49–54, 2000.

[30] C. Jacobsen, S. Williams, E. Anderson, M. Browne, C. Buckley, D. Kern, J. Kirz, M. Rivers, and X. Zhang, "Diffraction-limited imaging in a scanning transmission x-ray microscope," *Optics Communications*, vol. 86, no. 3-4, pp. 351 – 364, 1991.

[31] H. et al. *Ultramicroscopy*, vol. 107, p. 644, 2007.

[32] F. Brizuela, S. Carbajo, A. Sakdinawat, D. Alessi, D. H. Martz, Y. Wang, B. Luther, K. A. Goldberg, I. Mochi, D. T. Attwood, B. L. Fontaine, J. J. Rocca, and C. S. Menoni, "Extreme ultraviolet laser-based table-top aerial image metrology of lithographic masks," *Opt. Express*, vol. 18, pp. 14467–14473, Jul 2010.

[33] S. Rehbein, S. Heim, P. Guttmann, S. Werner, and G. Schneider, "Ultrahigh-resolution soft-x-ray microscopy with zone plates in high orders of diffraction," *Phys. Rev. Lett.*, vol. 103, p. 110801, Sep 2009.

[34] I. A. Artioukov, A. V. Vinogradov, V. E. Asadchikov, Y. S. Kas'yanov, R. V. Serov, A. I. Fedorenko, V. V. Kondratenko, and S. A. Yulin, "Schwarzschild soft-x-ray microscope for imaging of nonradiating objects," *Opt. Lett.*, vol. 20, pp. 2451–2453, Dec 1995.

[35] X. Zeng, F. Duewer, M. Feser, C. Huang, A. Lyon, A. Tkachuk, and W. Yun, "Ellipsoidal and parabolic glass capillaries as condensers for x-ray microscopes," *Appl. Opt.*, vol. 47, pp. 2376–2381, May 2008.

[36] C. A. Brewer, F. Brizuela, P. Wachulak, D. H. Martz, W. Chao, E. H. Anderson, D. T. Attwood, A. V. Vinogradov, I. A. Artyukov, A. G. Ponomareko, V. V. Kondratenko, M. C. Marconi, J. J. Rocca, and C. S. Menoni, "Single-shot extreme ultraviolet laser imaging of nanostructures with wavelength resolution," *Opt. Lett.*, vol. 33, pp. 518–520, Mar 2008.

[37] W. Chao, J. Kim, S. Rekawa, P. Fischer, and E. H. Anderson, "Demonstration of 12 nm resolution fresnel zone plate lens based soft x-ray microscopy," *Opt. Express*, vol. 17, pp. 17669–17677, Sep 2009.

[38] R. L. Sandberg, C. Song, P. W. Wachulak, D. A. Raymondson, A. Paul, B. Amirbekian, E. Lee, A. E. Sakdinawat, C. La-O-Vorakiat, M. C. Marconi, C. S. Menoni, M. M. Murnane, J. J. Rocca, H. C. Kapteyn, and J. Miao, "High numerical aperture tabletop soft x-ray diffraction microscopy with 70-nm resolution," *Proceedings of the National Academy of Sciences*, vol. 105, no. 1, pp. 24–27, 2008.

[39] A. B. et al., "Ultrafast single-shot diffraction imaging of nanoscale dynamics," *Nature Photonics*, vol. 2, pp. 415–419, 2008.

[40] S. M. et al., "Femtosecond time-delay x-ray holography," *Nature*, vol. 448, pp. 676–679, Aug 2011.

[41] I. M. . H. Kapteyn, "High-harmonic generation: Ultrafast lasers yield x-rays," *Nature Photonics*, vol. 4, pp. 149 – 151, 2010.

[42] D. Gabor, "A new microscope principle," *Nature*, vol. 161, pp. 777–778, May 1948.

[43] H. N. C. et al., "Femtosecond time-delay x-ray holography," *Nature*, vol. 448, pp. 676–679, Aug 2011.

[44] C. M. G. et al., "Sequential femtosecond x-ray imaging," *Nature Photonics*, vol. 5, pp. 99–102, Jan 2011.

[45] H. C. et al., "Ultrafast coherent diffractive imaging at flash," *Nat. Phys.*, vol. 2, no. 839, 2006.

[46] R. L. Sandberg, A. Paul, D. A. Raymondson, S. Hädrich, D. M. Gaudiosi, J. Holtsnider, R. I. Tobey, O. Cohen, M. M. Murnane, H. C. Kapteyn, C. Song, J. Miao, Y. Liu, and F. Salmassi, "Lensless diffractive imaging

using tabletop coherent high-harmonic soft-x-ray beams," *Phys. Rev. Lett.*, vol. 99, p. 098103, Aug 2007.

[47] M. et al., "Extending the methodology of x-ray crystallography to allow imaging of micromere-sized non-crystalline specimens," *Nature Photonics*, vol. 400, pp. 342 – 344, 1999.

[48] M. Bolte, G. Meier, B. Krüger, A. Drews, R. Eiselt, L. Bocklage, S. Bohlens, T. Tyliszczak, A. Vansteenkiste, B. Van Waeyenberge, K. W. Chou, A. Puzic, and H. Stoll, "Time-resolved x-ray microscopy of spin-torque-induced magnetic vortex gyration," *Phys. Rev. Lett.*, vol. 100, p. 176601, Apr 2008.

[49] K. E. et al., "Electromechanical transducers at the nanoscale: Actuation and sensing of motion in nanoelectromechanical systems (nems)," *Rev. Sci. Instrum.*, vol. 786, 2005.

[50] C. et al., "Clocking femtosecond x rays," *Phys. Rev. Lett.*, vol. 94, p. 114801, Mar 2005.

[51] G. Meier, M. Bolte, R. Eiselt, B. Krüger, D.-H. Kim, and P. Fischer, "Direct imaging of stochastic domain-wall motion driven by nanosecond current pulses," *Phys. Rev. Lett.*, vol. 98, p. 187202, May 2007.

[52] A. V. et al., "X-ray imaging of the dynamic magnetic vortex core deformation," *Nat. Phys.*, pp. 332–334, March 2009.

[53] S. Kasai, P. Fischer, M.-Y. Im, K. Yamada, Y. Nakatani, K. Kobayashi, H. Kohno, and T. Ono, "Probing the spin polarization of current by soft x-ray imaging of current-induced magnetic vortex dynamics," *Phys. Rev. Lett.*, vol. 101, p. 237203, Dec 2008.

[54] H. Jung, Y.-S. Yu, K.-S. Lee, M.-Y. Im, P. Fischer, L. Bocklage, A. Vogel, M. Bolte, G. Meier, and S.-K. Kim, "Observation of coupled vortex

gyrations by 70-ps-time- and 20-nm-space-resolved full-field magnetic transmission soft x-ray microscopy," *Applied Physics Letters*, vol. 97, no. 22, p. 222502, 2010.

[55] J. Wang, "Ultrafast x-ray imaging of fuel sprays," *AIP Conference Proceedings*, vol. 879, no. 1, pp. 1535–1538, 2007.

[56] H. N. C. et al., "Femtosecond diffractive imaging with a soft-x-ray free-electron laser," *Nature Physics*, vol. 2, pp. 839–463, 2006.

[57] M.-C. Chou, R.-P. Huang, P.-H. Lin, C.-T. Huang, S. yuan Chen, H.-H. Chu, J. Wang, and J.-Y. Lin, "Single-shot soft-x-ray digital holographic microscopy with an adjustable field of view and magnification," *Opt. Lett.*, vol. 34, pp. 623–625, Mar 2009.

[58] H. T. Kim, I. J. Kim, C. M. Kim, T. M. Jeong, T. J. Yu, S. K. Lee, J. H. Sung, J. W. Yoon, H. Yun, S. C. Jeon, I. W. Choi, and J. Lee, "Single-shot nanometer-scale holographic imaging with laser-driven x-ray laser," *Applied Physics Letters*, vol. 98, pp. 121105 –121105–3, mar 2011.

[59] A. Ravasio, D. Gauthier, F. R. N. C. Maia, M. Billon, J.-P. Caumes, D. Garzella, M. Géléoc, O. Gobert, J.-F. Hergott, A.-M. Pena, H. Perez, B. Carré, E. Bourhis, J. Gierak, A. Madouri, D. Mailly, B. Schiedt, M. Fajardo, J. Gautier, P. Zeitoun, P. H. Bucksbaum, J. Hajdu, and H. Merdji, "Single-shot diffractive imaging with a table-top femtosecond soft x-ray laser-harmonics source," *Phys. Rev. Lett.*, vol. 103, p. 028104, Jul 2009.

[60] O. Bostanjoglo and T. Rosin, "Ultrasonically induced magnetic reversals observed by stroboscopic electron microscopy," *Optica Acta*, vol. 24, no. 6, pp. 657–664.

[61] A. Zewail and J. Thomas, *4D Electron Microscopy: Imaging in Space and Time*. World Scientific Publishing Company, Incorporated, 2009.

[62] F. Carbone, O.-H. Kwon, and A. H. Zewail, "Dynamics of chemical bonding mapped by energy-resolved 4d electron microscopy," *Science*, vol. 325, no. 5937, pp. 181–184, 2009.

[63] M. R. Armstrong, K. Boyden, N. D. Browning, G. H. Campbell, J. D. Colvin, W. J. DeHope, A. M. Frank, D. J. Gibson, F. Hartemann, J. S. Kim, W. E. King, T. B. LaGrange, B. J. Pyke, B. W. Reed, R. M. Shuttlesworth, B. C. Stuart, and B. R. Torralva, "Practical considerations for high spatial and temporal resolution dynamic transmission electron microscopy," *Ultramicroscopy*, vol. 107, no. 4-5, pp. 356 – 367, 2007.

[64] M. R. Armstrong, B. W. Reed, B. R. Torralva, and N. D. Browning, "Prospects for electron imaging with ultrafast time resolution," vol. 90, no. 11, p. 114101, 2007.

[65] G. Binnig, H. Rohrer, C. Gerber, and E. Weibel, "Surface studies by scanning tunneling microscopy," *Phys. Rev. Lett.*, vol. 49, pp. 57–61, Jul 1982.

[66] Y. Martin, C. C. Williams, and H. K. Wickramasinghe, "Atomic force microscope: force mapping and profiling," *Journal of Applied Physics*, vol. 61, pp. 4723 –4729, may 1987.

[67] H. A. S. et al., "Protein-folding dynamics: Overview of molecular simulation techniques," *Review of Physical Chemistry*, vol. 58, pp. 57–83, 2006.

[68] V. Cosslett and W. Nixon, "X-ray microscopy," *Cambridge*, 1960.

[69] A. Baez *J. Opt. Soc. Am.*, vol. 42, 1952.

[70] B. N. et al. *Appl. Opt.*, vol. 15, 1976.

[71] B. N. et al. *Nucl. Instr. and Meth.*, vol. 208, 1983.

[72] B. N. et al. *Synchrotron Radiation Instrumentation, Stanford*, vol. 675, 1986.

[73] G. Schmahl and D. Rudolph, "X-ray microscopy," *Springer, Berlin*, 1984.

[74] P. Horowitz and J. Howell *Science*, vol. 608, 1972.

[75] O. von Hofsten, M. Bertilson, J. Reinspach, A. Holmberg, H. M. Hertz, and U. Vogt, "Sub-25-nm laboratory x-ray microscopy using a compound fresnel zone plate," *Opt. Lett.*, vol. 34, pp. 2631–2633, Sep 2009.

[76] M. Bertilson, O. von Hofsten, U. Vogt, A. Holmberg, and H. M. Hertz, "High-resolution computed tomography with a compact soft x-ray microscope," *Opt. Express*, vol. 17, pp. 11057–11065, Jun 2009.

[77] W. S. Haddad, I. McNulty, J. E. Trebes, E. H. Anderson, R. A. Levesque, and L. Yang, "Ultrahigh-resolution x-ray tomography," *Science*, vol. 266, no. 5188, pp. 1213–1215, 1994.

[78] S. E. et al., "Lensless imaging of magnetic nanostructures by x-ray spectroholography," *Nature*, vol. 432, pp. 885–888, July 2004.

[79] P. W. Wachulak, M. C. Marconi, R. A. Bartels, C. S. Menoni, and J. J. Rocca, "Soft x-ray laser holography with wavelength resolution," *J. Opt. Soc. Am. B*, vol. 25, pp. 1811–1814, Nov 2008.

[80] H. N. Chapman and K. A. Nuggent, "Coherent lensless x-ray imaging," *Nature Photonics*, vol. 4, pp. 833–839, November 2010.

[81] W. J. Huang, J. M. Zuo, B. Jiang, K. W. Kwon, and M. Shim, "Sub-angstrom-resolution diffractive imaging of single nanocrystals," *Nature Physics*, vol. 5, pp. 129–133, Nov 2009.

[82] H. M. Q. et al., "Diffractive imaging of highly focused x-ray fields," *Nature Physics*, vol. 2, pp. 101–104, 2006.

[83] M. D. Seaberg, D. E. Adams, E. L. Townsend, D. A. Raymondson, W. F. Schlotter, Y. Liu, C. S. Menoni, L. Rong, C.-C. Chen, J. Miao, and et al., "Ultrahigh 22 nm resolution coherent diffractive imaging using a desktop 13 nm high harmonic source," *Optics Express*, vol. 19, no. 23, p. 22470, 2011.

[84] T. Warwick, H. Ade, A. P. Hitchcock, H. Padmore, E. Rightor, and B. P. Tonner, "Soft x-ray spectromicroscopy development for materials science at the advanced light source," *Journal of Electron Spectroscopy and Related Phenomena*, vol. 84, no. 1-3, pp. 85 – 98, 1997.

[85] P. Fischer, G. Denbeaux, T. Ono, T. Okuno, T. Eimller, D. Goll, and G. Schtz, "Study of magnetic domains by magnetic soft x-ray transmission microscopy," *Journal of Physics D: Applied Physics*, vol. 35, no. 19, p. 2391, 2002.

[86] S. Kasai, P. Fischer, M.-Y. Im, K. Yamada, Y. Nakatani, K. Kobayashi, H. Kohno, and T. Ono, "Probing the spin polarization of current by soft x-ray imaging of current-induced magnetic vortex dynamics," *Phys. Rev. Lett.*, vol. 101, p. 237203, Dec 2008.

[87] P. G. O'Shea and H. P. Freund, "Free-electron lasers: Status and applications," *Science*, vol. 292, no. 5523, pp. 1853–1858, 2001.

[88] W. Meyer-Ilse, T. Warwick, and D. Attwood, *X-ray microscopy: proceedings of the sixth international conference, Berkeley, CA, 2-6 August 1999*. Review of progress in quantitative nondestructive evaluation, American Institute of Physics, 2000.

[89] "http://flash.desy.de/."

[90] P. Schmueser, M. Dohlus, and J. Rossbach, *Ultraviolet and soft X-ray free-electron lasers: introduction to physical principles, experimental results, technological challenges*. Springer tracts in modern physics, Springer, 2008.

[91] A. Rubenchik and S. Witkowski, *Physics of Laser Plasma*. Elsevier, 1991.

[92] R. Fabbro, J. Fournier, P. Ballard, D. Devaux, and J. Virmont, "Physical study of laser x2010;produced plasma in confined geometry," *Journal of Applied Physics*, vol. 68, pp. 775 –784, jul 1990.

[93] J. J. Rocca, V. Shlyaptsev, F. G. Tomasel, O. D. Cortázar, D. Hartshorn, and J. L. A. Chilla, "Demonstration of a discharge pumped table-top soft-x-ray laser," *Phys. Rev. Lett.*, vol. 73, pp. 2192–2195, Oct 1994.

[94] J. Rocca, M. Marconi, J. Chilla, D. Clark, F. Tomasel, and V. Shlyaptsev, "Discharge-driven 46.9-nm amplifier with gain-length approaching saturation," *Selected Topics in Quantum Electronics, IEEE Journal of*, vol. 1, pp. 945 –948, sep 1995.

[95] F. Tomasel, J. Rocca, and V. Shlyaptsev, "Dynamics of the plasma column of a capillary discharge soft x-ray laser," *Plasma Science, IEEE Transactions on*, vol. 24, pp. 49 –50, feb 1996.

[96] M. Frati, M. Seminario, and J. J. Rocca, "Demonstration of a 10-μj tabletop laser at 52.9 nm in neonlike chlorine," *Opt. Lett.*, vol. 25, pp. 1022–1024, Jul 2000.

[97] Y. Liu, M. Seminario, F. Tomasel, C. Chang, J. Rocca, and D. Attwood, "Achievement of essentially full spatial coherence in a high-average-power soft-x-ray laser," *Physical Review A*, vol. 63, Feb. 2001.

[98] A. Isoyan, F. Jiang, Y. C. Cheng, F. Cerrina, P. Wachulak, L. Urbanski, J. Rocca, C. Menoni, and M. Marconi, "Talbot lithography: Self-imaging of complex structures," vol. 27, no. 6, pp. 2931–2937, 2009.

[99] J. J. Rocca, C. H. Moreno, M. C. Marconi, and K. Kanizay, "Soft-x-ray laser interferometry of a plasma with a tabletop laser and a lloyd's mirror," *Opt. Lett.*, vol. 24, pp. 420–422, Mar 1999.

[100] J. Filevich, K. Kanizay, M. C. Marconi, J. L. A. Chilla, and J. J. Rocca, "Dense plasma diagnostics with an amplitude-division soft-x-ray laser interferometer based on diffraction gratings," *Opt. Lett.*, vol. 25, pp. 356–358, Mar 2000.

[101] F. Brizuela, G. Vaschenko, C. Brewer, M. Grisham, C. Menoni, M. Marconi, J. Rocca, W. Chao, J. Liddle, E. Anderson, D. Attwood, A. Vinogradov, I. Artioukov, Y. Pershyn, and V. Kondratenko, "Reflection mode imaging with nanoscale resolution using a compact extreme ultraviolet laser," *Opt. Express*, vol. 13, pp. 3983–3988, May 2005.

[102] P. W. Wachulak, M. G. Capeluto, M. C. Marconi, C. S. Menoni, and J. J. Rocca, "Patterning of nano-scale arrays by table-top extreme ultraviolet laser interferometric lithography," *Opt. Express*, vol. 15, pp. 3465–3469, Mar 2007.

[103] G. Vaschenko, A. G. Etxarri, C. S. Menoni, J. J. Rocca, O. Hemberg, S. Bloom, W. Chao, E. H. Anderson, D. T. Attwood, Y. Lu, and B. Parkinson, "Nanometer-scale ablation with a table-top soft x-ray laser," *Opt. Lett.*, vol. 31, pp. 3615–3617, Dec 2006.

[104] B. J. MacGowan, L. B. D. Silva, D. J. Fields, C. J. Keane, J. A. Koch, R. A. London, D. L. Matthews, S. Maxon, S. Mrowka, A. L. Osterheld, J. H. Scofield, G. Shimkaveg, J. E. Trebes, and R. S. Walling, "Short wavelength x-ray laser research at the lawrence livermore national laboratory," vol. 4, no. 7, pp. 2326–2337, 1992.

[105] S. Sebban, T. Mocek, D. Ros, L. Upcraft, P. Balcou, R. Haroutunian, G. Grillon, B. Rus, A. Klisnick, A. Carillon, G. Jamelot, C. Valentin, A. Rousse, J. P. Rousseau, L. Notebaert, M. Pittman, and D. Hulin, "Demonstration of a ni-like kr optical-field-ionization collisional soft x-ray laser at 32.8 nm," *Phys. Rev. Lett.*, vol. 89, p. 253901, Nov 2002.

[106] M.-C. Chou, P.-H. Lin, C.-A. Lin, J.-Y. Lin, J. Wang, and S.-Y. Chen, "Dramatic enhancement of optical-field-ionization collisional-excitation x-ray lasing by an optically preformed plasma waveguide," *Phys. Rev. Lett.*, vol. 99, p. 063904, Aug 2007.

[107] D. Zimmer, B. Zielbauer, M. Pittman, O. Guilbaud, J. Habib, S. Kazamias, D. Ros, V. Bagnoud, and T. Kuehl, "Optimization of a tabletop high-repetition-rate soft x-ray laser pumped in double-pulse single-beam grazing incidence," *Opt. Lett.*, vol. 35, pp. 450–452, Feb 2010.

[108] J. J. Rocca, Y. Wang, M. A. Larotonda, B. M. Luther, M. Berrill, and D. Alessi, "Saturated 13.2 nm high-repetition-rate laser in nickellike cadmium," *Opt. Lett.*, vol. 30, pp. 2581–2583, Oct 2005.

[109] D. Alessi, D. H. Martz, Y. Wang, M. Berrill, B. M. Luther, and J. J. Rocca, "Gain-saturated 10.9 nm tabletop laser operating at 1 hz repetition rate," *Opt. Lett.*, vol. 35, pp. 414–416, Feb 2010.

[110] D. H. Martz, D. Alessi, B. M. Luther, Y. Wang, D. Kemp, M. Berrill, and J. J. Rocca, "High-energy 13.9 nm table-top soft-x-ray laser at 2.5 hz repetition rate excited by a slab-pumped ti:sapphire laser.," *Optics Letters*, vol. 35, no. 10, pp. 1632–1634, 2010.

[111] J. Tümmler, R. Jung, H. Stiel, P. V. Nickles, and W. Sandner, "High-repetition-rate chirped-pulse-amplification thin-disk laser system with joule-level pulse energy," *Opt. Lett.*, vol. 34, pp. 1378–1380, May 2009.

[112] F. J. Furch, B. A. Reagan, B. M. Luther, A. H. Curtis, S. P. Meehan, and J. J. Rocca, "Demonstration of an all-diode-pumped soft x-ray laser," *Opt. Lett.*, vol. 34, pp. 3352–3354, Nov 2009.

[113] P. Zeitoun, G. Faivre, S. Sebban, T. Mocek, A. Hallou, M. Fajardo, D. Aubert, P. Balcou, F. Burgy, D. Douillet, and et al., "A high-intensity highly coherent soft x-ray femtosecond laser seeded by a high harmonic beam," *Nature*, vol. 431, no. 7007, pp. 426–429, 2004.

[114] Y. Wang, E. Granados, M. A. Larotonda, M. Berrill, B. M. Luther, D. Patel, C. S. Menoni, and J. J. Rocca, "High-brightness injection-seeded soft-x-ray-

laser amplifier using a solid target," *Phys. Rev. Lett.*, vol. 97, p. 123901, Sep 2006.

[115] F. Pedaci, Y. Wang, M. Berrill, B. Luther, E. Granados, and J. J. Rocca, "Highly coherent injection-seeded 13.2 nm tabletop soft x-ray laser," *Opt. Lett.*, vol. 33, pp. 491–493, Mar 2008.

[116] M. H. et al., "Attosecond metrology," *Nature*, vol. 414, pp. 509–513, Nov 2001.

[117] E. Goulielmakis, V. S. Yakovlev, A. L. Cavalieri, M. Uiberacker, V. Pervak, A. Apolonski, R. Kienberger, U. Kleineberg, and F. Krausz, "Attosecond control and measurement: Lightwave electronics," *Science*, vol. 317, no. 5839, pp. 769–775, 2007.

[118] C. T. et al., "Plasma mirrors for ultrahigh-intensity optics," *Nature Physics*, vol. 3, pp. 424–429, 2007.

[119] K. Z. Hatsagortsyan, M. Klaiber, C. Müller, M. C. Kohler, and C. H. Keitel, "Laser-driven relativistic recollisions," *J. Opt. Soc. Am. B*, vol. 25, pp. B92–B103, Jul 2008.

[120] A. Rundquist, C. G. Durfee, Z. Chang, C. Herne, S. Backus, M. M. Murnane, and H. C. Kapteyn, "Phase-matched generation of coherent soft x-rays," *Science*, vol. 280, no. 5368, pp. 1412–1415, 1998.

[121] C. G. Durfee, A. R. Rundquist, S. Backus, C. Herne, M. M. Murnane, and H. C. Kapteyn, "Phase matching of high-order harmonics in hollow waveguides," *Phys. Rev. Lett.*, vol. 83, pp. 2187–2190, Sep 1999.

[122] R. A. Bartels, A. Paul, H. Green, H. C. Kapteyn, M. M. Murnane, S. Backus, I. P. Christov, Y. Liu, D. Attwood, and C. Jacobsen, "Generation of spatially coherent light at extreme ultraviolet wavelengths," *Science*, vol. 297, no. 5580, pp. 376–378, 2002.

[123] R. B. et al., "Shaped-pulse optimization of coherent emission of high-harmonic soft x-ryas," *Nature*, vol. 406, pp. 164–166, 2000.

[124] J. A. Armstrong, N. Bloembergen, J. Ducuing, and P. S. Pershan, "Interactions between light waves in a nonlinear dielectric," *Phys. Rev.*, vol. 127, pp. 1918–1939, Sep 1962.

[125] T. Popmintchev, M.-C. Chen, A. Bahabad, M. Gerrity, P. Sidorenko, O. Cohen, I. P. Christov, M. M. Murnane, and H. C. Kapteyn, "Phase matching of high harmonic generation in the soft and hard x-ray regions of the spectrum," *Proceedings of the National Academy of Sciences*, vol. 106, no. 26, pp. 10516–10521, 2009.

[126] B. Henke, E. Gullikson, and J. Davis, *X-ray interactions: photoabsorption, scattering, transmission, and reflection at E.* Atomic data and nuclear data tables, Academic Press, 1993.

[127] "http://www.esrf.eu/computing/scientific/xop2.1/extensions.html."

[128] C. M. et al., "Multilayer reflective coatings for extreme-ultraviolet lithography," *SPIE Proceedings*, vol. 42, p. 3331, 1998.

[129] "http://www.cxro.lbl.gov/."

[130] Y. Uspenskii, V. E. Levashov, A. V. Vinogradov, A. I. Fedorenko, V. V. Kondratenko, Y. Pershin, E. N. Zubarev, and V. Y. Fedotov, "High-reflectivity multilayer mirrors for a vacuum-ultraviolet interval of 35-50nm," *Opt. Lett.*, vol. 23, pp. 771–773, May 1998.

[131] R. Soufli, R. M. Hudyma, E. Spiller, E. M. Gullikson, M. A. Schmidt, J. C. Robinson, S. L. Baker, C. C. Walton, and J. S. Taylor, "Sub-diffraction-limited multilayer coatings for the 0.3 numerical aperture micro-exposure tool for extreme ultraviolet lithography," *Appl. Opt.*, vol. 46, pp. 3736–3746, Jun 2007.

[132] A. Aquila, F. Salmassi, Y. Liu, and E. Gullikson, "Tri-material multilayer coatings with high reflectivity and wide bandwidth for 25 to 50 nm extreme ultraviolet light," *Opt. Express*, vol. 17, pp. 22102–22107, Nov 2009.

[133] M.-H. Hu, K. L. Guen, J.-M. Andre, P. Jonnard, S. K. Zhou, H. C. Li, J. T. Zhu, and Z. S. Wang, "Co/mg/x multilayer mirrors for the euv range," *AIP Conference Proceedings*, vol. 1221, no. 1, pp. 56–58, 2010.

[134] D. L. W. et al., "Euv multilayers for solar physics," *SPIE Proceedings*, vol. 5168, no. 1, 2004.

[135] M. Suman, G. Monaco, M.-G. Pelizzo, D. L. Windt, and P. Nicolosi, "Realization and characterization of an xuvmultilayer coating for attosecond pulses," *Opt. Express*, vol. 17, pp. 7922–7932, May 2009.

[136] A. Wonisch, U. Neuhäusler, N. M. Kabachnik, T. Uphues, M. Uiberacker, V. Yakovlev, F. Krausz, M. Drescher, U. Kleineberg, and U. Heinzmann, "Design, fabrication, and analysis of chirped multilayer mirrors for reflection of extreme-ultraviolet attosecond pulses," *Appl. Opt.*, vol. 45, pp. 4147–4156, Jun 2006.

[137] J. Kirz, "Phase zone plates for x rays and the extreme uv," *J. Opt. Soc. Am.*, vol. 64, pp. 301–309, Mar 1974.

[138] J. Goodman, *Introduction to Fourier optics*. McGraw-Hill physical and quantum electronics series, Roberts & Co., 2005.

[139] A. Kozmat and C. R. Christensent, "Effects of speckle on resolution," *J. Opt. Soc. Am.*, vol. 66, pp. 1257–1260, Nov 1976.

[140] S. Heinbuch, M. Grisham, D. Martz, and J. J. Rocca, "Demonstration of a desk-top size high repetition rate soft x-ray laser," *Opt. Express*, vol. 13, pp. 4050–4055, May 2005.

[141] E. H. Anderson, "Specialized electron beam nanolithography for euv and x-ray diffraction optics," *IEEE J. Quantum Electronics*, vol. 27, no. 42, 2006.

[142] J. J. Rocca, V. Shlyaptsev, F. G. Tomasel, O. D. Cortázar, D. Hartshorn, and J. L. A. Chilla, "Demonstration of a discharge pumped table-top soft-x-ray laser," *Phys. Rev. Lett.*, vol. 73, pp. 2192–2195, Oct 1994.

[143] Y. Liu, M. Seminario, F. Tomasel, C. Chang, J. Rocca, and D. Attwood, "Achievement of essentially full spatial coherence in a high-average-power soft-x-ray laser," *PHYSICAL REVIEW A*, vol. 63, MAR 2001.

[144] D. V. et al., "Structural transformations in sc/si multilayers irradiated by euv lasers," *Lawrence Berkeley National Laboratory*, 2008.

[145] I. A. Artioukov, R. M. Fechtchenko, A. L. Udovskii, Y. A. Uspenskii, and A. V. Vinogradov, "Soft x-ray multilayer mirrors based on depleted uranium," *Nuclear Instruments and Methods in Physics Research Section A: Accelerators, Spectrometers, Detectors and Associated Equipment*, vol. 517, no. 1-3, pp. 372 – 377, 2004.

[146] J. Cazaux, "A physical approach to the radiation damage mechanisms induced by x-rays in x-ray microscopy and related techniques," *Journal of Microscopy*, vol. 188, no. 2, pp. 106–124, 1997.

[147] H. Fujisaki, S. Takahashi, H. Ohzeki, K. Sugisaki, H. Kondo, H. Nagata, H. Kato, and S. Ishiwata, "Soft-x-ray damage to biological samples," *Journal of Microscopy*, vol. 182, no. 2, pp. 79–83, 1996.

[148] M. C. Downer, R. L. Fork, and C. V. Shank, "Femtosecond imaging of melting and evaporation at a photoexcited silicon surface," *J. Opt. Soc. Am. B*, vol. 2, pp. 595–599, Apr 1985.

[149] V. V. Temnov, K. Sokolowski-Tinten, P. Zhou, and D. von der Linde, "Ultrafast imaging interferometry at femtosecond-laser-excited surfaces," *J. Opt. Soc. Am. B*, vol. 23, pp. 1954–1964, Sep 2006.

[150] O.-H. Kwon, V. Ortalan, and A. H. Zewail, "Macromolecular structural dynamics visualized by pulsed dose control in 4d electron microscopy.," *Proceedings of the National Academy of Sciences of the United States of America*, vol. 108, no. 15, pp. 6026–6031, 2011.

[151] M. L. Taheri, T. Lagrange, B. W. Reed, M. R. Armstrong, G. H. Campbell, W. J. DeHope, J. S. Kim, W. E. King, D. J. Masiel, and N. D. Browning, "Laser-based in situ techniques: Novel methods for generating extreme conditions in tem samples," *Microscopy Research and Technique*, vol. 72, pp. 122–130, 2009.

[152] B. A. et al., "Lensless imaging using broadband x-ray sources," *Nature Photonics*, vol. 5, pp. 420–424, Jun. 2011.

[153] C. A. Brewer, G. Vaschenko, F. Brizuela, Y. Wang, M. A. Larotonda, B. M. Luther, M. C. Marconi, J. J. Rocca, C. S. Menoni, W. Chao, J. A. Liddle, Y. Liu, E. H. Anderson, and D. T. Attwood, "Sub-38 nm resolution microscopy with a tabletop 13 nm wavelength laser," *Conference on Lasers and Electro-Optics/Quantum Electronics and Laser Science Conference and Photonic Applications Systems Technologies*, p. CME4, 2006.

[154] M.-C. Chou, R.-P. Huang, P.-H. Lin, C.-T. Huang, S. yuan Chen, H.-H. Chu, J. Wang, and J.-Y. Lin, "Single-shot soft-x-ray digital holographic microscopy with an adjustable field of view and magnification," *Opt. Lett.*, vol. 34, pp. 623–625, Mar 2009.

[155] A. V. Z. A. Hendrych, R. Kubinek, "The magnetic force microscopy and its capability for nano-magnetic studies - the short compendium," *Modern Research and Educational Topics in Microscopy*, pp. 805–811.

[156] J. Teva, G. Abadal, Z. Davis, J. Verd, X. Borris, A. Boisen, F. Prez-Murano, and N. Barniol, "On the electromechanical modelling of a resonating nanocantilever-based transducer," *Ultramicroscopy*, vol. 100, no. 3-4, pp. 225 –

232, 2004. ¡ce:title¿Proceedings of the Fifth International Conference on Scanning Probe Micrscopy, Sensors and Nanostructures¡/ce:title¿.

[157] G. Abadal, Z. J. Davis, B. Helbo, X. Borris, R. Ruiz, A. Boisen, F. Campabadal, J. Esteve, E. Figueras, F. Prez-Murano, and N. Barniol, "Electromechanical model of a resonating nano-cantilever-based sensor for high-resolution and high-sensitivity mass detection," *Nanotechnology*, vol. 12, no. 2, p. 100, 2001.

[158] D. H. Martz, D. Alessi, B. M. Luther, Y. Wang, D. Kemp, M. Berrill, and J. J. Rocca, "High-energy 13.9 nm table-top soft-x-ray laser at 2.5 hz repetition rate excited by a slab-pumped ti:sapphire laser," *Opt. Lett.*, vol. 35, pp. 1632–1634, May 2010.

[159] Y. Wang, M. Larotonda, B. Luther, D. Alessi, M. Berrill, V. N. Shlyaptsev, and J. J. Rocca, "Demonstration of high-repetition-rate tabletop soft-x-ray lasers with saturated output at wavelengths down to 13.9 nm and gain down to 10.9 nm," *Physical Review A*, vol. 72, no. 5, pp. 1–7, 2005.

[160] "http://www.nist.gov/mml/metallurgy/magneticsrms.cfm."

[161] Y. L. et al. *Adv. Func. Mat.*, vol. 21, 2011.

[162] K. Williams, K. Gupta, and M. Wasilik, "Etch rates for micromachining processing-part ii," *Microelectromechanical Systems, Journal of*, vol. 12, pp. 761 – 778, dec. 2003.

Appendix A

Sample holders

Silicon nitride water chambers have traditionally been utilized to hold a wet sample as intact as possible in a vacuum environment. Much higher efficiency can be achieved, specially for lower photon energies in the SXR region, by replacing the silicon nitride for a silicon layer. Two alternative approaches towards increasing the throughput of these chamber will be assessed in this section.

A.0.3 Stratified a-Si Chambers

The illustration in figure A.1 summarizes the layout of the membrane design and constitution, from bottom to the top.

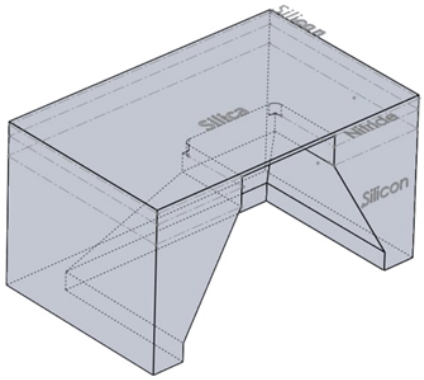

Figure A.1: oblique view of the design of the cavity where the biological specimen are sealed.

- **Silicon Nitride (Si_3N_4) -** As an electrical insulator with a good thermal

shock resistance, high fracture toughness and outstanding wear resistance, the main purpose of the layers of silicon nitride is to yield the structure with a robust and reliable hermetic seal, providing advanced protection to other deposited film layers. Frequently, and specially in this case, it is necessary to use high fracture toughness silicon nitride to allow an appropriate interlayer shape.

- **Crystalline Silicon (Si) -** This layer is the substrate of the membrane and is processed from a crystalline silicon wafer form. The crystal orientation is <100> as defined by the Miller index, which leads to a single crystal's highly anisotropic structural and electronic properties combination. This orientation is extremely related to the wafer cleavage directions and other material manipulation factors.

- **Silicon Oxide ($a - SiO_2$) -** Silica is a group IV metal oxide, which exhibits good abrasion resistance, electrical insulation and high thermal stability. It is insoluble in all acids with the exception of hydrogen fluoride (HF). That is why it serves as a convenient dielectric interlayer in the design. In other words, the interface between silica and silicon plays an important role in the fabrication of the windows since HF does not attack silicon.

- **Amorphous Silicon ($a - Si$) -** Maximum uniformity is required for this layer as it is the only layer separating the medium where the specimen is immersed and the vacuum. Small variations in the flatness of this film may cause strong scattering.

Fabrication Process

The a-Si-based membranes are manufactured following standard microfabrication procedures of the semiconductor industry. It starts with p-type doped 2" diameter silicon wafers, <100> oriented, several tens of microns thick (typically 100 - 200 μm) and nominal resistivity of about 1-40 Ω. A layer of silicon nitride

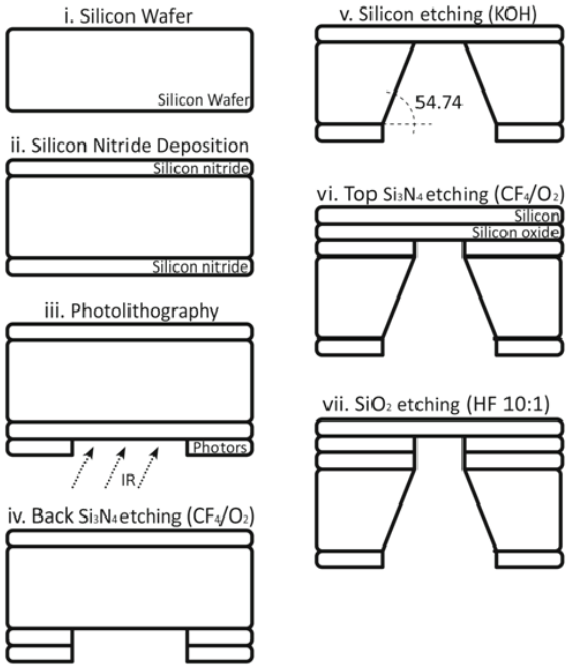

(Si_3N_4) of thickness 300 nm is deposited on both sides of the wafer by low pressure chemical vapor deposition (LPCVD) at around 100 mTorr (820 C). Afterwards, the backside Si_3N_4 layer is patterned according to the design using photo-lithographic techniques on a standard positive photo-resist. After the development, the pattern is transferred to a reactive ion etcher (RIE) in order to etch the backside nitride layer using an adequate concentration of any fluoride-based plasma (CF_4/O_2 or SF_6/O_2) at an optimized pressure and power. The remaining nitride layer serves as a mask, so that the Si substrate is anisotropically etched in potassium hydroxide (KOH). The following step of the process is a sputter deposition of a few tens of nanometers of silica onto the top nitride layer through ion beam sputtering (IBS). The last layer of Si of thickness equal to the desired membrane thickness (a few tens of nanometers) is also deposited using the same method. Subsequently, the top nitride layer is also removed through a fluoride-based reactive back-etching under the same conditions as those for the backside layer due to the symmetry of the structure. Finally, in order to produce a single Si layer membrane on top of the sample the silica layer is etched with buffered (usually 10:1) hydrogen fluoride.

Photolithographic Development

The photolithographic process begins with a deposition of photoresist on the backside silicon nitride film. To that end, the entire wafer is carefully cleaned with solvents and pre-baked on a hot plate at 120 C for 2 minutes to make sure that all the remaining solvent has evaporated before the photoresist deposition. Then, the positive photoresist Shipley 1818 coats the upper face of the wafer using a spin-coater at 4000 RPM for 30 seconds, resulting in a 23 kÅ thickness film. To conclude the deposition of the photoresist, the wafer is baked for 90 sec at a 95 C temperature. Thereafter, the wafer is aligned with the corresponding mask using a manual mask and exposed for 11 seconds at a UV illumination power of 15 mW/cm^2. Finally, the wafer is developed to remove the exposed zones of the photoresist with a 4:1 solution of distilled water and 400K developer for 45 seconds.

Photomask

Ultimately, the design of the photomask will only depend on the desired cavity shape and dimensions. In photolithography for semiconductor production, it is common practice to use a chromium mask as a light shield, which is a chromium film specifically patterned on a quartz substrate. The patterning of a chromium film can usually be roughly summarized in a photolithography process consisting of forming a quartz substrate with a chromium film, coating the chromium film with a resist film, and forming a resist pattern by pattering the resist film with an electron beam. These masks are usually 4" $\times$ 4" $\times$ 0.09" in dimension.

Silicon Nitride Dry Etching

Once the photoresist deposited onto the backside silicon nitride layer has been patterned, the wafer is transferred to the reactive ion etcher (RIE) to proceed with the etching of the nitride layer. A basic RIE consists of a set of parallel electrodes within a cylindrical vacuum chamber. Generally, the sample is loaded onto the

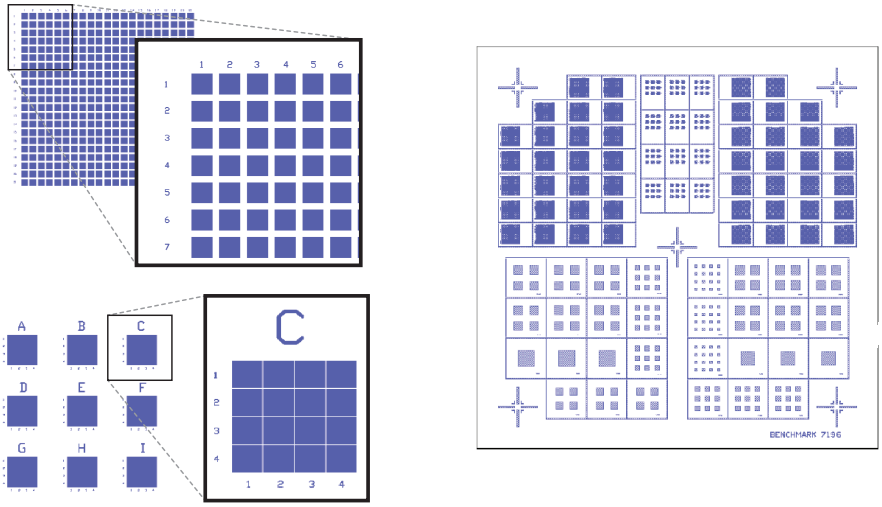

grounded electrode of the RIE in order to electrically isolate it from the rest of the chamber when the desired gas flow and power are set to create the appropriate conditions for the plasma. For this process, two calibrations were realized for a CF_4/O_2 gas flows under very similar conditions.

	Calibration 1	Calibration 2
CF_4 concentration	40 sccm	32 sccm
O_2 concentration	6 sccm	8 sccm
P before plasma	10 mTorr	14 mTorr
P after plasma	80 mTorr	125 mTorr
Power	40 W	40 W
Etch Rate	**1.72 nm/s**	**1.25 nm/sec**

Silicon Wet Etching

The remaining patterned silicon nitride on the wafer backside serves as a mask for the wet etching, allowing KOH to etch anisotropically the opened squares and lines. Silicon <100> is typically anisotropically etched with a KOH hot bath giving an etching angle of 54.74 degrees with respect to the layer parallel plane. The bath is maintained at a constant temperature of 85 C using a close loop temperature-control hot plate. The KOH solution ought to contain a proportion of 2.5 L H_2O per 1 kg KOH pellets.

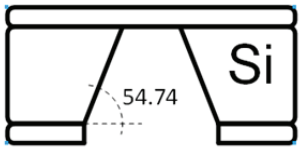

Figure A.2: Etching of <100> silicon in a KOH bath

After the solution has been stabilized at the desired temperature, the sample is immersed into the KOH for several tens of minutes supported by a Teflon holder. This configuration is calibrated to provide an etch rate of **16.78 nm/s** on a <100> Si layer. During the process, the solution must be stirred to prevent air bubbles from disrupting the uniformity of the etching. Finally, the sample is quickly removed from the KOH bath and neutralized to stop the reaction in reduced hydrochloric acid (1:1 HCl/H_2O).

a-Silica and a-Silicon Deposition

Both depositions are carried out using an Ion Beam Sputtering (IBS) system. Ar is introduced into the discharge chamber, where energetic electrons from a cathode strike and ionize Ar atoms. A set of grids set a -1 kV potential difference used to accelerate ions. The Ar neutrals of high kinetic energy collide with the target, producing a plasma that travels towards the sample and deposits on its surface. The IBS system has typically been calibrated for 150 nm silica and 80 nm silicon depositions at around 100 C. The specific deposition rates are relatively low, 15.36 nm/min and 20 nm/min for silica and silicon, respectively.

Silica Wet Etching

The grown silica layer acts as an isolator for the final Si-based membrane. Since hydrofluoric acid (HF) has a very high selectivity over silicon, it is the most appropriate etcher to allow silicon to remain intact, as the membrane homogeneity is critical for imaging. HF can be very dangerous if mishandled. In addition, because the etch rate is a function of the solution pH, buffered HF has a much

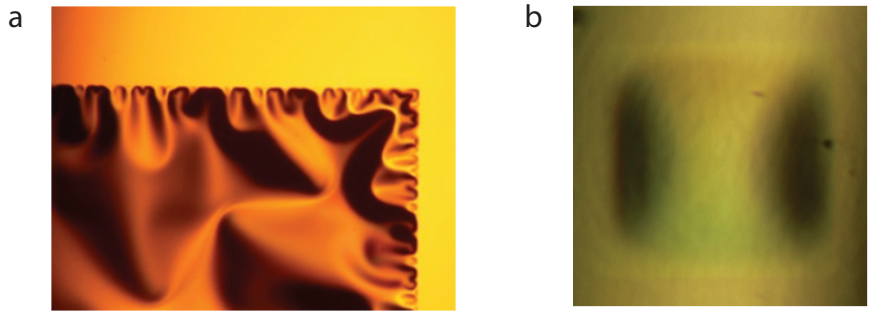

Figure A.3: **a,** 1 mm wide square edge after silicon and silicon oxide deposition (post-annealing). **b,** Dark-field image of a 10 μm wide silicon membrane.

more controlled etch rate over other etchers. For that, the solution used for the etching is a buffered HF 10:1, enabling a slower etch rate, but still quite repeatable, remaining constant even after a large number of samples have been etched. Consequently, as timing for this etching is not as critical as within the process of membrane fabrication, no accurate calibration is required. In general, standard etch-rates are tabulated by Williams et al. for further reference [162].

Fabrication Defects

One of the most critical factors during the fabrication is the final membrane roughness and stress, which has a direct effect on the their flatness. Annealing can partially mitigate stress, although ripples are accentuated for larger membrane areas. For best results, annealing must be performed at several hundreds of degree Celsius with minimized thermal-shock (slow ramp-up/-down).

A.0.4 B-doped Si Chambers

Selective etching of silicon can be provide the same desired outcome as in the previously described fabrication process, although greatly reducing the stress on the final window. Channelling of ethylenediamine and pyrocatechol (EDP) is achieved by grading p-dopant (typically Boron) diffusion and density on silicon, since EDP will not attack silicon with concentrations above $7 \times 10^{19}\ B/cm^2$. Therefore, the final window thickness will depend on the depth inside silicon that falls above that

number. B-dopant grading is done by implant with ranging energies from 30 to 50 keV depending on the desired thickness, within a few hundreds of nanometers for B.

EDP is the most selective etchant for this procedure, it exhibits a <111>:<100> anisotropy of 1:35, although it is highly corrosive and carcinogenic. The recipe consists of 1 L ethylenediamine + 160 g pyrocatechol, 6 g pyrazine soluted in 133 mL H_2O, leading to etch rates

70 C	14 $\mu m/hr$
80 C	20 $\mu m/hr$
90 C	30 $\mu m/hr$
95 C	14 $\mu m/hr$

EDP etching can result in deposits of polymerized $Si(OH)_4$ on etched silicon surfaces. In order to avoid it, a post-EDP protocol needs to follow as

1. 20 seconds in DI water.
2. 120 second dip in 5 % ascorbic acid (vitamin C) + DI water.
3. 120 second rinse in DI water.
4. 60 second dip in hexane (C_6H_{14}).

This recipe is planned to be implemented in the near future. A more extensive assessment of its results and capabilities will then proceed.